RESEARCH ARTICLE SUMMARY

IMMUNOLOGY

KLF2 maintains lineage fidelity and suppresses CD8 T cell exhaustion during acute LCMV infection

Eric Fagerberg, John Attanasio, Christine Dien, Jaiveer Singh, Emily A. Kessler, Leena Abdullah, Jian Shen, Brian G. Hunt, Kelli A. Connolly, Edward De Brouwer, Jiaming He, Nivedita R. Iyer, Jessica Buck, Emily R. Borr, Martina Damo, Gena G. Foster, Josephine R. Giles, Yina H. Huang, John S. Tsang, Smita Krishnaswamy, Weiguo Cui, Nikhil S. Joshi*

INTRODUCTION: Naïve CD8 T cells have the potential to differentiate into a variety of effector and memory CD8 T cell states during an immune response. These states reflect the cells' functional potential to fight infection, respond to immunotherapies, or cause immunopathology. Acute T cell responses are associated with highly functional effector and memory states. Conversely, chronic antigen environments, as seen in tumors and chronic infection, drive dysfunctional T cell fate decisions, termed generally as T cell exhaustion.

RATIONALE: Despite recent insights into how these divergent T cell differentiation states determine physiological outcomes, it remains uncertain how fate decisions are made and what mechanisms exist to suppress differentiation towards alternative fates and maintain lineage fidelity. High-dimensional single-cell studies have enabled deep inquiry into the spectrum of T cell differentiation states across different immune challenges, and, from this, efforts have been made to infer differentiation trajectories and their underlying transcriptional regulation. Yet, testing these predictions has traditionally been accomplished through lower-throughput knock-out and/or lineage-tracing experiments. PerturbSEQ is a technique that couples CRISPR perturbations of target genes with single-cell RNA sequencing (scRNA-seq) and enables mechanistic dissection of differentiation processes. In this study, we used perturbSEQ with the goal of understanding factors that regulate fate decisions and preserve T cell lineage fidelity.

RESULTS: We generated a differentiation space map (DSM) of the spectrum of CD8 T cell states in acute and chronic lymphocytic choriomeningitis virus (LCMV) infection across time points using scRNA-seq. Analyses across four time points revealed a linear differentiation trajectory in acute infection, whereas a bifurcation between effector and exhausted trajectories was observed in chronic infection. We then performed in vivo perturbSEQ in LCMV-specific CD8 T cells for a library of ~40 genes [largely transcription factors (TFs) and epigenetic modulators] in the context of acute LCMV infection. This experiment identified proteins that could regulate the extent to which cells differentiated along an expected memory to effector trajectory, thereby highlighting their role as a suppressor or promoter of specific T cell functions. Moreover, it elucidated KLF2 as a transcription factor that maintains effector lineage fidelity. KLF2 knockout (KO) T cells aberrantly acquired distinct features of exhaustion during acute LCMV infection. This included impaired effector and memory differentiation and function during both primary and secondary viral challenge. Epigenetic changes, both at sites of KLF2 binding and globally throughout the genome, overlapped with loci accessibility changes seen in chronic infection. Mechanistic studies showed that KLF2 was downregulated upon T cell receptor stimulation and was intrinsically required for suppression of the exhaustion-defining TF, TOX. Epistasis experiments revealed that KLF2 was also critical for enabling the function of the effector-defining TF, TBET. Investigation in tumor models pointed to a role for KLF2 in the early bifurcation of effector and exhausted differentiation trajectories as KLF2 was required to maintain a polyfunctional TCF1$^+$ CD62L$^+$ precursor state. KO cells less potently controlled tumors and exhibited enhanced differentiation with features of exhaustion and residence. Overexpression of KLF2 was sufficient to rescue this precursor state in tumor-draining lymph nodes as well as suppress features of exhaustion and induce effector differentiation in acute and chronic viral infection.

CONCLUSION: Our study highlighted the role of many TFs in regulating the extent to which CD8 T cells differentiate along a defined linear trajectory and revealed KLF2's distinct role in enabling cells to remain on this effector lineage. This adds to our mechanistic understanding of T cell fate decisions and demonstrates that differentiation toward the exhaustion lineage is suppressed in acute infection. It additionally opens new questions regarding maintenance of lineage fidelity across immune contexts, where little is still known. Further, modulation of KLF2 proved useful in driving or suppressing distinct T cell functional states with potential implications for immunotherapy. ∎
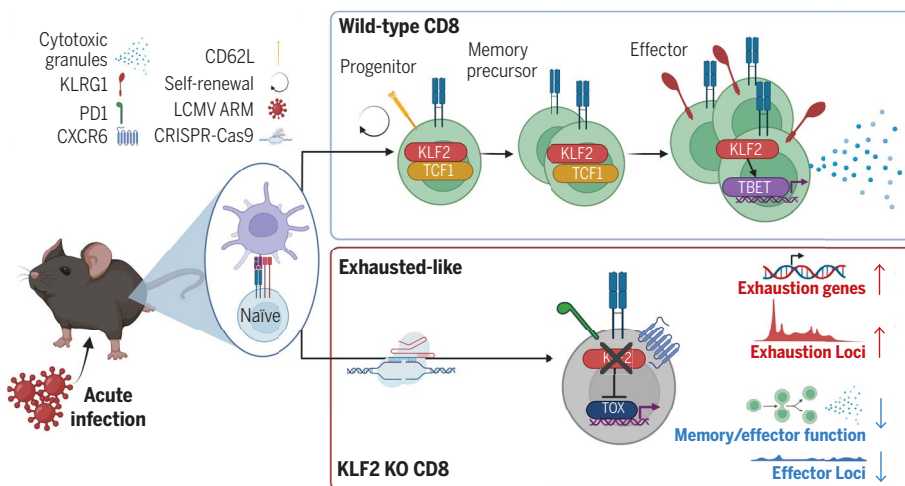
KLF2 prevents aberrant CD8 T cell differentiation in acute LCMV infection. Naïve CD8 T cells undergo functional effector differentiation in acute LCMV infection. This effector differentiation involves KLF2-dependent TBET activity. KLF2 KO in this setting results in aberrant CD8 T cell differentiation to a TOX$^+$ exhausted-like state. This is characterized by an epigenetic and transcriptional signature resembling hallmark features of CD8 T cells in chronic infection and results in reduced cytolytic potential and memory recall capacity. [Figure created with BioRender.com]

READ THE FULL ARTICLE AT
https://doi.org/10.1126/science.adn2337

RESEARCH ARTICLE

IMMUNOLOGY

KLF2 maintains lineage fidelity and suppresses CD8 T cell exhaustion during acute LCMV infection

Eric Fagerberg[1], John Attanasio[1], Christine Dien[1,2], Jaiveer Singh[1], Emily A. Kessler[1], Leena Abdullah[3], Jian Shen[4], Brian G. Hunt[1], Kelli A. Connolly[1], Edward De Brouwer[5]†, Jiaming He[1], Nivedita R. Iyer[1], Jessica Buck[1], Emily R. Borr[1], Martina Damo[6], Gena G. Foster[7], Josephine R. Giles[8,9,10], Yina H. Huang[3], John S. Tsang[1,11,12,13], Smita Krishnaswamy[3,14,15], Weiguo Cui[4], Nikhil S. Joshi[1]*

Naïve CD8 T cells have the potential to differentiate into a spectrum of functional states during an immune response. How these developmental decisions are made and what mechanisms exist to suppress differentiation toward alternative fates remains unclear. We employed in vivo CRISPR-Cas9–based perturbation sequencing to assess the role of ~40 transcription factors (TFs) and epigenetic modulators in T cell fate decisions. Unexpectedly, we found that knockout of the TF *Klf2* resulted in aberrant differentiation to exhausted-like CD8 T cells during acute infection. KLF2 was required to suppress the exhaustion-promoting TF TOX and to enable the TF TBET to drive effector differentiation. KLF2 was also necessary to maintain a polyfunctional tumor-specific progenitor state. Thus, KLF2 provides effector CD8 T cell lineage fidelity and suppresses the exhaustion program.

A pool of heterogeneous effector CD8 T cells is generated during infections and cancer, and this heterogeneity comprises cells with varying propensities for an array of functional attributes, including survival, self-renewal, proliferation, resilience to repeated antigen challenge, migration into tissues, residence in lymphoid organs, cytokine production, and killing (*1–6*). At the peak of acute lymphocytic choriomeningitis virus (LCMV) infection, at least two subsets of CD8 T cells can be distinguished: less-differentiated memory precursors (Tmpecs) and terminally differentiated effectors (Teffs), with Tmpecs giving rise to Teffs. Tmpec cells have potential for survival, self-renewal, proliferation, and cytokine production (*7–9*), whereas Teff cells produce high levels of cytolytic effector proteins [granzymes A and B (GzmA and GzmB), perforin] with the trade-off of low proliferative capacity and longevity. However, dependent on the type of challenge and signals present, different CD8 T cell states will be generated, each possessing distinct combinations of these canonical features (*10–15*). A naïve CD8 T cell has the potential to differentiate into any of these states (*16–18*), and the prevailing model for how this occurs is that integration of signals present during a challenge will alter CD8-T-cell developmental trajectories through modulation of transcription factors (TFs) and epigenetic modifiers (EMs) (*3, 19–25*). Yet, questions remain regarding how lineage fidelity is maintained during different challenges.

Data generated from individual T cells in different situations may be used to create a "differentiation space map" (DSM) that reflects the relationships between T cell states in different conditions, facilitating the prediction of differentiation trajectories and estimation of the relative importance of individual TFs and EMs for a given trajectory (*18, 26, 27*). In this work, we constructed a DSM and used perturbSEQ to investigate the roles of 39 TFs and EMs during the in vivo differentiation of effector CD8 T cells in acute LCMV infection. PerturbSEQ combines CRISPR-Cas9–based gene editing and single-cell RNA sequencing (scRNA-seq) and allowed us to test the relative importance of these factors in the CD8 T cell effector differentiation process (*28–32*).

Results

Generating a map of CD8 T cell differentiation space in acute and chronic LCMV infection

PerturbSEQ data can be mapped onto a DSM, which allows unexpected differentiation states to be revealed. We set out to create a DSM that would encompass most of the achievable differentiation states for splenic CD8 T cells in LCMV infection. The CD8 T cell responses to acute (Armstrong strain) and chronic (Clone 13 strain) LCMV infections peaks at day 8, then T cell numbers contract, stabilizing after day 30. Virus is cleared from the spleen by days 6 and 40 in Armstrong and Clone 13, respectively (*33*). Thus, we reasoned that analysis of cells between days 4 and 40 would encompass most of the possible splenic CD8 T cell differentiation states in LCMV. We performed scRNA-seq on endogenous GP33-specific CD8 T cells sorted from the spleens of C57Bl/6 mice on days 4, 8, 28, and 40 after infection with acute and chronic LCMV (Fig. 1A). After preprocessing, we performed integration, dimensionality reduction, and clustering to visualize the data in two-dimensional (2D) and 3D uniform manifold approximation and projection (UMAP) plots (Fig. 1, B and C, and fig. S1A). Notably, we observed that CD8 T cells substantially differed along three axes: UMAP1, corresponding to genes associated with T cell progenitor and differentiated states; UMAP2, corresponding to activated and resting states; and UMAP3, corresponding to effector and exhausted states (fig. S1B).

We validated the 11 DSM clusters by visualizing their respective differentially expressed genes (DEGs) and enrichment for previously published gene signatures (fig. S1, C and D, and data S1) (*18*). Analyses of the different time points showed that cell states were not fixed, as distinct clusters were enriched at different timepoints. Additionally, differences between acute and chronic infection could be observed as early as day 4, when, for example, *Tox*-expressing exhausted progenitor (Texprog, also known as stem-like) cells were present in chronic LCMV– but not acute LCMV–infected mice (Fig. 1D and fig. S1E). These differences became more pronounced on days 8 and 28 but abated between days 28 and 40, in line with viral clearance from the spleen.

It was important to then understand how differentiation trajectories dictated cell fates in both infections, including the relationship between cell states, to make predictions about genes underlying these processes. We defined the precursor cluster as the starting point for cells in both acute and chronic LCMV and performed pseudotime analyses to predict differentiation trajectories. Analyses on cells from acute LCMV revealed a dominant linear "Acute effector" differentiation trajectory (Fig. 1E and fig. S1, F to H). Cells moved from a precursor to memory precursor (Tmpec) state before terminally differentiating at the Teff cluster. At day 4 of acute infection, we also observed cells occupying a transient activation and proliferative state in the exhausted-intermediate (Texint) and interferon (IFN)–stimulated (Tisg) clusters

[1]Department of Immunobiology, Yale University School of Medicine, New Haven, CT, USA. [2]Program in Computational Biology & Bioinformatics, Yale University, New Haven, CT, USA. [3]Department of Microbiology and Immunology, Geisel School of Medicine at Dartmouth, Lebanon, NH, USA. [4]Department of Pathology, Feinberg School of Medicine at Northwestern University, Chicago, IL, USA. [5]Department of Genetics and Computer Science, Yale University School of Medicine, New Haven, CT, USA. [6]Department of Medicine, University of Chicago, Chicago, IL, USA. [7]Section of Hematology, Department of Internal Medicine, Yale University School of Medicine, New Haven, CT, USA. [8]Department of Systems Pharmacology and Translational Therapeutics, University of Pennsylvania, Philadelphia, PA, USA. [9]Institute for Immunology, Perelman School of Medicine, University of Pennsylvania, Philadelphia, PA, USA. [10]Parker Institute for Cancer Immunotherapy, Perelman School of Medicine, University of Pennsylvania, Philadelphia, PA, USA. [11]Yale Center for Systems and Engineering Immunology, Yale University School of Medicine, New Haven, CT, USA. [12]Chan Zuckerberg Biohub New York, New York, NY, USA. [13]Department of Biomedical Engineering, Yale University, New Haven, CT, USA. [14]Computational Biology and Bioinformatics Program, Yale University, New Haven, CT USA. [15]Applied Math Program, Yale University, New Haven, CT, USA.

*Corresponding author. Email: nikhil.joshi@yale.edu
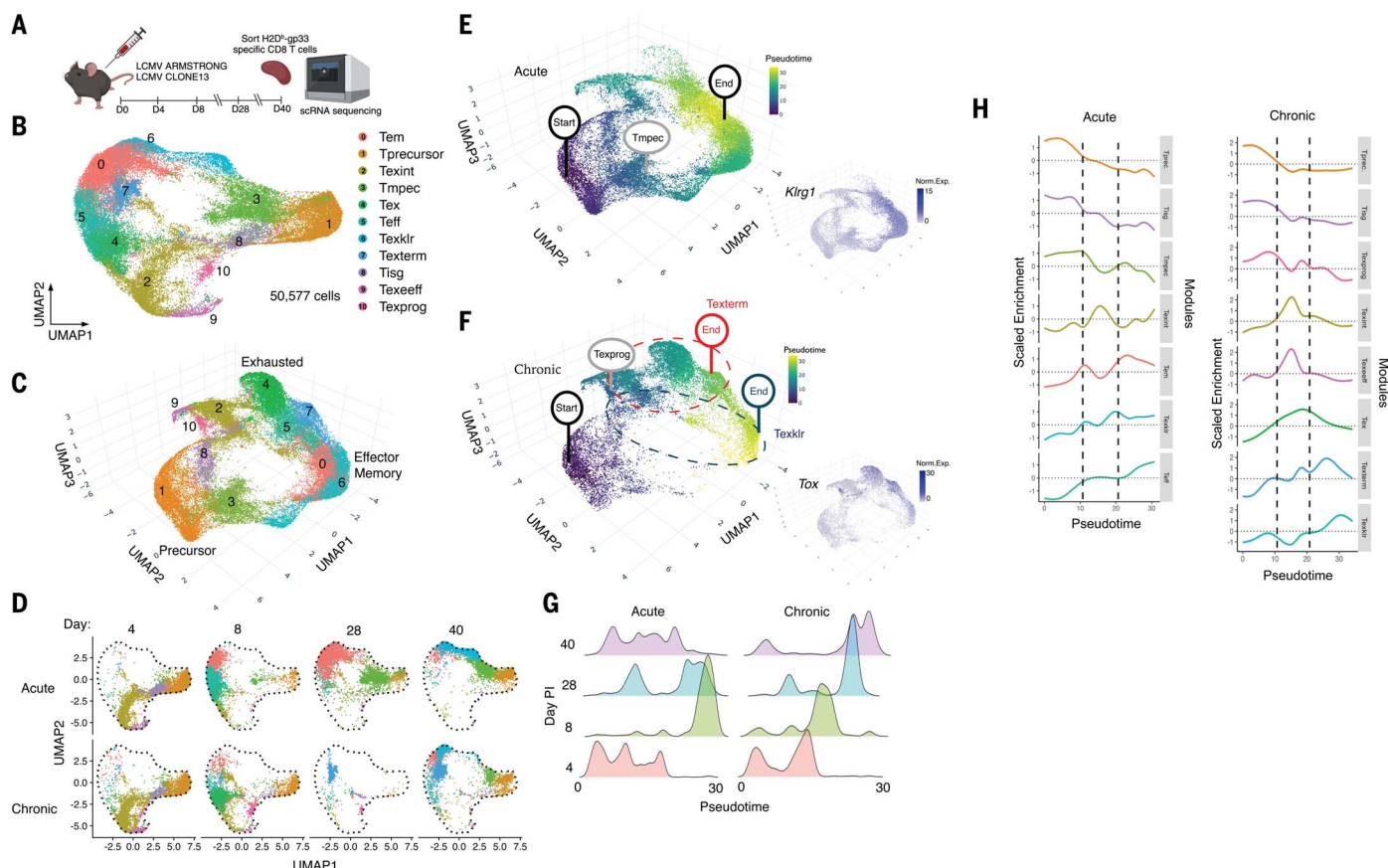†Present address: Genentech, San Francisco, CA, US.

Fig. 1. scRNA-seq generates map of distinct differentiation trajectories in acute and chronic infection. (**A**) Mice were infected with either acute or chronic LCMV followed by sorting of antigen-specific CD8 T cells from the spleen at the specified timepoints for scRNA-seq. *n* = 5 to 10 mice pooled for each time point; staggered infection to sort on same day. (**B**) UMAP reduction of all LCMV samples (50,577 cells) highlighting clusters identified. (**C**) 3D UMAP reduction highlighting UMAP3 as the dimension separating effector and exhausted cells. (**D**) Relative distribution of cells across timepoints and infections. (**E**) Monocle pseudotime trajectory of all cells in acute infection. Norm.Exp., normalized expression. (**F**) Monocle pseudotime trajectory of all cells in chronic infection. (**G**) Abundance of cells from each time point over pseudotime. PI, postinfection. (**H**) Gene modules were derived from each cluster, and relative cell enrichment for each module was plotted over pseudotime for both acute and chronic trajectories.

(Fig. 1D and fig. S1E). There is a 10-fold contraction of effector CD8 T cells after day 8 of acute LCMV infection with preferential survival of less-differentiated cells to form memory (*34*, *35*), and we saw corresponding shifts from the Teff cluster to the effector memory (Tem), Tmpec, and precursor clusters between days 8 and 40. Visualization of pseudotime distributions by actual time showed pseudotime peaking at day 8 and then regressing between days 8 to 40 (Fig. 1G), in line with preferential survival of these less-differentiated cell clusters.

Analyses of cells from chronic infection revealed an initial trajectory from precursor to Tisg to Texprog before bifurcating into distinct "chronic effector" (Texklr) and "chronic exhaustion" trajectories (Tex or Texterm) (Fig. 1F and fig. S1H). Exhausted early-effectors (Texeeffs) were enriched at day 4 and resembled an early activation state that gives rise to Texprog cells (10) in chronic infection (*18*, *36*). Notably, the TF Tox, necessary for the development of ex-

hausted cells (*37–39*), was expressed throughout the chronic exhaustion trajectory (Fig. 1F, inset). Visualization of pseudotime distributions by actual time supported progressive differentiation of cells in chronic infection in contrast to those in acute infection (Fig. 1G), and comparison of prominent gene modules further highlighted differences between infections (Fig. 1H). These data were consistent with prior work that suggests that resting Texprog cells (10) give rise to a proliferative intermediate (2) followed by further differentiation into Texklr (6) and/or Texterm cells (7). However, analyses of our DSM could not determine whether these lineages converge at a later point (*i.e.*, whether Texklr cells give rise to Texterm cells) (*25*). Our data were more consistent with the bifurcated trajectory described previously (*18*, *40*, *41*), and we considered these two distinct pathways downstream of the Texprog state. Together, these analyses provided a framework to ask questions regarding the role of specific TFs and EMs and enabled a deeper

interpretation of our subsequent perturbSEQ experiments.

Performing perturbSEQ on select TFs and EMs in acute LCMV infection

We selected a pool of candidate genes and performed perturbSEQ in virus-specific CD8 T cells during acute LCMV. We chose 25 TFs, 7 EMs, and 7 other genes of interest, many of which have already been implicated in T cell differentiation. This included a panel of 14 TFs that we identified as differentially expressed along the axis of effector T cell differentiation in cancer and 25 genes curated from our DSM and CD8 T cell literature (*42*) (Fig. S2, A and B). We created a library containing three single-guide RNAs (sgRNAs) per gene and six nontargeting control sgRNAs (sgNTCs), which comprised 15% of the total sgRNA pool (data S2). The sgRNA sequences were designed to include a 10× Genomics handle and was cloned into a retroviral backbone driving expression of human CD2 (hCD2) as a selection marker (fig. S3A).

P14 Cas9+ CD8 T cells were activated and transduced and reliably expressed hCD2 proportional to the amount of virus used (fig. S3B), enabling subsequent magnetic enrichment (fig. S3C). Additionally, the modified sgRNAs were functional, as *Thy1* targeting sgRNA successfully resulted in protein knockdown (fig. S3D).

To perform perturbSEQ in vivo, dsRED+ Cas9+ P14 CD8 T cells were transduced at a low multiplicity of infection, positively selected on hCD2, and transferred into day 1 acute LCMV-infected congenic recipients (Fig. 2A). At day 8 after infection, spleens were harvested, and P14s and endogenous H2Db-gp33 specific CD8 T cells were sorted (fig. S3E). Endogenous GP33-specific T cells were spiked into the sorted P14 CD8 T cells at a 1:10 ratio, and 5′ 10× Genomics–based scRNA-seq was performed. After preprocessing and filtering the data, we conclusively assigned sgRNAs against every target gene in the library (fig. S3, F and G, and data S3). Recovery of sgNTC cells was at the expected frequency, whereas there was variability in the recovery of experimental sgRNAs. We also noted variable correlations between the perturbation and the expression of the target gene (fig. S3H), consistent with Cas9-based knockout (KO) not resulting in complete disruption of the mRNA (43, 44). Lastly, comparison of DEGs between endogenous T cells (control) and sgNTC dsRED+ P14 CD8 T cells showed minimal differences (fig. S3I), suggesting that the perturbSEQ control (unedited) P14 cell states resembled the endogenous day 8 effector T cell response.

We visualized the perturbSEQ data with 2D and 3D UMAP plots and identified seven perturbSEQ clusters that we classified based on DEGs (Fig. 2B, fig. S4, A and B, and data S4). We observed similar patterns of expression for representative Tmpec and Teff cell markers (*Il7r*, *Tcf7*, *Cxcr3*, *Klrg1*, *Cx3cr1*, and *Gzma*) in the perturbSEQ clusters and day 8 LCMV Armstrong cells (fig. S4C), and this was reflective of protein expression in vivo (fig. S4, D and E). Gene modules for the Tprecursor, Tex-like, and Teff perturbSEQ clusters were projected onto the DSM to confirm that the clusters were representative of their corresponding DSM cell states (Fig. 2C). The alignment was even more stringent when analysis focused only on DSM cells present at day 8 of acute or chronic LCMV infection (Fig. 2D and fig. S4F). Notably, DSM states found primarily in chronic infection (Texint, Tex, and Texterm) had strong enrichment for the perturbSEQ Tex-like module, highlighting a potential alternative fate in our acute infection dataset (Fig. 2, C and D).

Next, we assessed the distribution of the individual KO cells across the seven perturbSEQ clusters. The distribution of cells with control sgRNAs was as expected in an acute infection, with most of the control cells being classified into clusters of the effector trajectory (fig. S5A and data S3). Most KO cells also followed this

trend, although their distribution differed by target. *Klf2* KO cells were a notable exception, as they were primarily enriched in the Tex-like cluster, suggesting aberrant differentiation away from the effector trajectory (data S3).

To visualize population shifts, we generated density plots for the relative distribution of KO cells on the perturbSEQ UMAP plot (Fig. 2E). KOs could be divided into those that resulted in increased Tprecursor and Tmpec cells and those that increased Teff cells. Consistent with previous studies (8, 36, 45–55), loss of *Tbx21* (TBET), *Prdm1* (BLIMP1), *Id2*, *Tet2*, *Zeb2*, or *Ikzf1* increased Tprecursor and Tmpec cells, and deficiency of *Bach2*, *Lef1*, *Tcf7* (TCF1) or *Ezh2* promoted Teff cells. A strength of perturbSEQ is the ability to compare the relative impact of KOs, which allowed us to score each perturbation for enrichment of our DSM gene modules (Fig. 2F and fig. S5B), as well as our perturbSEQ-derived Teff and Tprecursor modules (fig. S5C). Analysis of the 11 gene modules from the DSM showed that *Klf2* KO cells had strong enrichment for the progenitor and exhausted modules and reduced enrichment for the effector and memory modules. Visualization of effector molecule expression further revealed perturbation-specific effects (fig. S5D).

Gene expression kinetics can often correlate with a gene's role in differentiation, and so we conducted RNA velocity analysis to visualize transcript dynamics of the genes we knocked out in our study (Fig. 2G). Many did not show highly specific regions of increased velocity, as measured by the unspliced/spliced mRNA ratio (fig. S5E). Notably, *Tcf7* and *Zeb2* had distinct areas of high transcript velocity in the Tprecursor and Teff clusters, respectively, highlighting their dynamic and important role in enforcing and maintaining these cell states (Fig. 2H). Despite *Tbx21* having a similar expression pattern to *Zeb2*, its velocity signature was more evenly distributed across clusters perhaps reflecting its biological role throughout effector and memory differentiation (Fig. 2H).

Pseudotime analyses of the perturbSEQ dataset revealed two differentiation trajectories: an effector trajectory (trajectory 1) that went from cluster 4-Tprecursor to cluster 1-Teff and an exhausted trajectory (trajectory 2) that went from 4-Tprecursor to 3-Tex-like (Fig. 2I). This sharp bifurcation was also visualized by using a second dimensionality reduction method, PHATE (fig. S5F) (56). DEGs between the Tprecursor and Teff clusters revealed expected genes, such as *Tcf7*, *Il7r*, and *Id3* (Tprecursor) as well as *Gzma*, *Klrg1*, and *Zeb2* (Teff), whereas differences between Tex-like and Tprecursor clusters (3 and 4) showed increased expression of genes associated with exhaustion (*Pdcd1*, *Cd160*, *Cd7*, and *Plac8*) and tissue residence [*Zfp683* (Hobit) and *Cxcr6*] (fig. S5, G and H). We then visualized the distribution of KO cells for each target along pseudotime (Fig. 2J and fig. S5I). To-

gether, these data were consistent with the idea that different TF or EM KOs led to an enrichment of cells at various points along the effector trajectory (with the notable exception of *Klf2*), consistent with there being discrete transition states rather than one continuously differentiating population.

Lef1 is less well studied than many of the other TFs in our screen and was expressed highest in Tprecursors and Tmpecs (fig. S6A). To determine whether LEF1 was necessary to retain less-differentiated cell states, we generated naïve *Lef1*-deficient P14 CD8 T cells using CRISPR-Cas9 editing and tested a 1:1 mixture of *Lef1* KO and control cells in B6 recipients infected with LCMV Armstrong. At day 8, *Lef1* KOs were highly enriched in Teff cells compared with Tmpec cells, as shown by the increased frequency of interleukin (IL)–7Rlo CX3CR1hi KLRG1+ CD8 T cells, an increased frequency of GzmA+ cells, and a decreased frequency of cells producing both tumor necrosis factor–α (TNF-α) and IFN-γ, all phenotypes and functional outcomes of Teff cell differentiation (fig. S6, B to E).

KLF2 KO T cells acquire features of exhaustion observed in chronic infection

KLF2 loss during acute infection resulted in a substantial increase in cells classified within the Tex-like cluster (Fig. 2E and fig. S5A). To further explore this result, we generated a *Klf2* KO gene expression module and projected it onto the DSM and found the highest enrichment in cells of the exhaustion lineage (Fig. 3A, fig. S7A, and data S5). Conversely, *Klf2* regulon activity was highest in the Teff, Tem, and Texklr clusters (Fig. 3B and fig. S7B). We further predicted how the KO cells would cluster on the DSM and observed a prevalence of exhausted cell states compared with control cells (fig. S7C). We saw enrichment of *Klf2* KO cells compared with control cells for Texprog, Tex, Texterm, and tissue resident memory (Trm) (57) gene modules (Fig. 3C). In addition, KOs showed up-regulation of Texterm genes and down-regulation of Texklr genes (fig. S7D), using DEGs previously defined in the literature (26).

To understand which features of exhaustion were KLF2-dependent or independent we compared DEGs of KO versus control cells in the perturbSEQ to DEGs from day 8 chronic versus acute infection (DSM) and found overlap, including up-regulation of *Tox*, *Tigit*, *Cd7*, *Cd160*, *P2rx7*, and *Plac8* as well as down-regulation of *Ccl5*, *Klrg1*, *Zeb2*, *S1pr5*, *Gzma*, and *Prf1* (fig. S7F and data S6). Notable exceptions included the up-regulation of *Zfp683*, *Id2*, and *Cxcr3*, only in KOs, and the up-regulation of *Havcr2*, *Xcl1*, *Irf8*, and *Nr4a1*, only in chronic infection.

We then used Cas9 RNPs to knock out KLF2 in naïve P14 CD8 T cells and studied their responses to acute LCMV infection (Fig. 3D and

Fig. 2. In vivo perturbSEQ reveals two trajectories of differentiation in acute infection. (**A**) PerturbSEQ workflow. P14 Cas9 T cells were transduced with sgRNA library and transferred into acute LCMV–infected mice. P14s were sorted and sequenced 8 days later. N = 8 mice from same infection cohort pooled prior to sort. (**B**) UMAP plot highlighting identified clusters. (59,815 cells). (**C**) Gene module enrichment of perturbSEQ clusters projected on Fig. 1 LCMV map. (**D**) Tex-like cluster gene module enrichment on cells from day 8 Arm or CL13 infection. (**E**) Density plots highlighting the relative enrichment of perturbations across clusters. (**F**) Perturbed cells were scored for gene module enrichment on the basis of those modules defined in Fig. 1. (**G**) RNA velocities determined by scVelo are projected as streamlines on the pertubSEQ UMAP. (**H**) RNA velocity of selected genes showing unspliced versus spliced mRNA counts (colored by cluster) and velocity projected onto the perturbSEQ UMAP compared with expression dynamics. Log. Norm., log normalized expression. (**I**) Monocle pseudotime analysis shows two distinct trajectories of differentiation projected onto 2D and 3D UMAP reductions. (**J**) Ridge plots showing the impact of perturbations on the degree to which cells differentiate along pseudotime. Statistical significance of mean from negative control mean was calculated by the Wilcoxon rank sum test. *$P < 0.05$; ***$P < 0.001$; ****$P < 0.0001$.
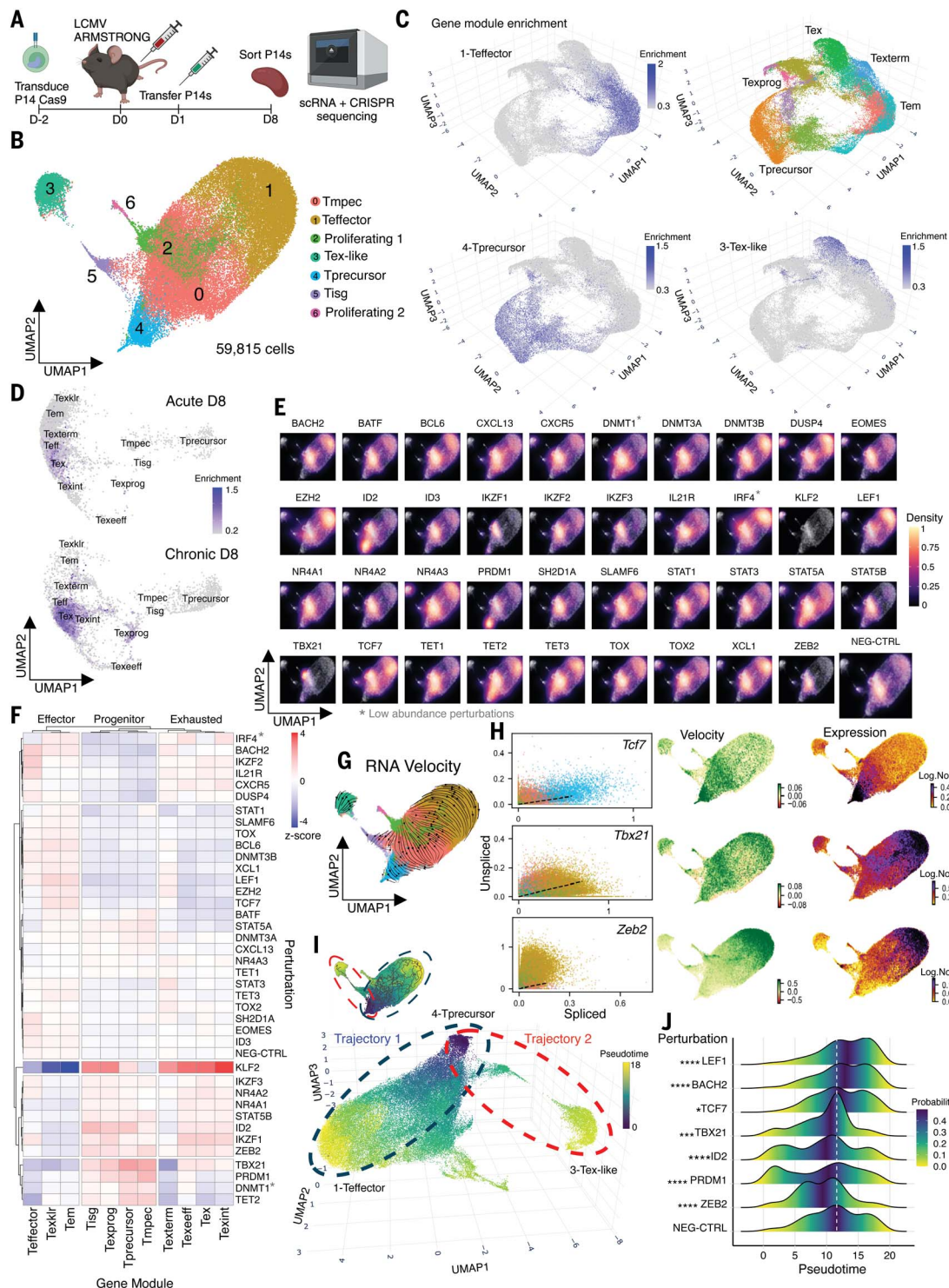
fig. S8A). At day 8, there were fewer IL-7R^lo CX3CR1^hi Teff cells (fig. S8B). Because KLF2 is thought to regulate *Cx3cr1* directly (*58*, *59*), we also examined IL-7R and KLRG1, a canonical effector gene (Fig. 3E). KLF2 KO cells were unable to produce GzmA or Perforin (Fig. 3F) but did produce GzmB, IFN-γ, and TNF-α in response to ex vivo gp33 peptide stimulation, although they did produce less IFN-γ on a per–

cell basis and more TNF-α as a population compared with control cells (fig. S8C).

In addition to the defects in effector differentiation, KLF2 KOs upregulated several proteins associated with exhausted T cells, including CD160, PD-1, TOX, and CXCR6 (Fig. 3G and fig. S8D). This was validated by comparison to endogenous gp33-specific CD8s from day 8 acute and chronic LCMV infection (Fig. 3H

and fig. S8D). Notably, wild-type (WT) P14 CD8 T cells at day 8 of LCMV Clone 13 could also produce IFN-γ and, to a lesser extent, TNF-α but had reduced GzmA expression relative to CD8 T cells in acute infection (fig. S8E). KO phenotypes were consistent with two independent *Klf2*-targeting sgRNAs (fig. S9).

Epigenetic changes are instrumental in orchestrating T cell differentiation processes

Fig. 3. KLF2 KO CD8 T cells acquire features of exhaustion in acute infection. (**A**) Gene module enrichment of KLF2 KO DEGs projected on Fig. 1 LCMV map. (**B**) Enrichment for KLF2 regulon (expression of predicted target genes) on Fig. 1 LCMV map. (**C**) Cells with KLF2-targeted or non-targeting sgRNAs were scored for enrichment of selected gene modules. The Trm module was derived from the literature (57). (**D**) Schematic of validation workflow; congenically distinct naïve P14s were isolated and electroporated with Cas9 RNPs prior to 50:50 mixing and transfer of 10,000 cells into day −1 LCMV ARM–infected mice. (**E**) Phenotype of KLF2 KO and control cells isolated from the spleen at day 8 after infection with LCMV ARM; TCF1 expression of CD127+ cells. N = 10 mice replicates, representative of three independent experiments. (**F**) Functional effector molecule expression of KLF2 KO and control cells isolated from spleens at day 8 after infection with LCMV ARM. N = 10 to 15 mice replicates, combined or representative data from three independent experiments. (**G**) Further phenotypic characterization of KLF2 KO cells compared with controls isolated from spleen at day 8 after infection with LCMV ARM showing several effector and exhaustion proteins. N = 8 to 18 mice replicates, data combined or representative of three independent experiments. (**H**) Phenotypic comparison of endogenous H2Db-gp33–specific CD8 T cells isolated from the spleens of mice at day 8 after infection with either LCMV ARM or LCMV CL13. Data is representative of two independent experiments. (**I**) KLF2 KO and control cells were sorted from spleens at day 8 after infection with LCMV ARM (KO and control) or LCMV CL13 (control). Heatmaps show relative accessibility of effector or exhaustion peaks in KO and control cells from acute infection; the nearest annotated genes are shown in boxes. N = 10 to 20 mice pooled prior to sort for each condition, two technical replicates for each sample. (**J**) Chromatin accessibility at selected effector specific or exhaustion specific loci. Representative plots shown for each sample of two technical replicates. All flow plots were pregated on live P14s unless indicated, representative gating scheme shown in fig. S8A; paired t tests were used to find statistical significance of flow data. ***P < 0.001; ****P < 0.0001; individual data points each represent one mouse with the connecting line indicating paired samples as KO and WT cotransfers were performed.

(18, 26, 60). To understand the impact of KLF2 KO on the epigenetic state of T cells in acute infection, we performed assay for transposase-accessible chromatin using sequencing (ATAC-seq) on KO P14 T cells from day 8 acute infection

and compared them with WT P14 T cells from day 8 acute and chronic infection (fig. S10A). Principal component analysis (PCA) highlighted high-level differences between the three samples and showed strong concordance between

replicates (fig. S10B). We determined differentially accessible loci between control cells from acute and chronic infection to generate a set of effector loci (more accessible in acute) and exhaustion loci (more accessible in chronic).
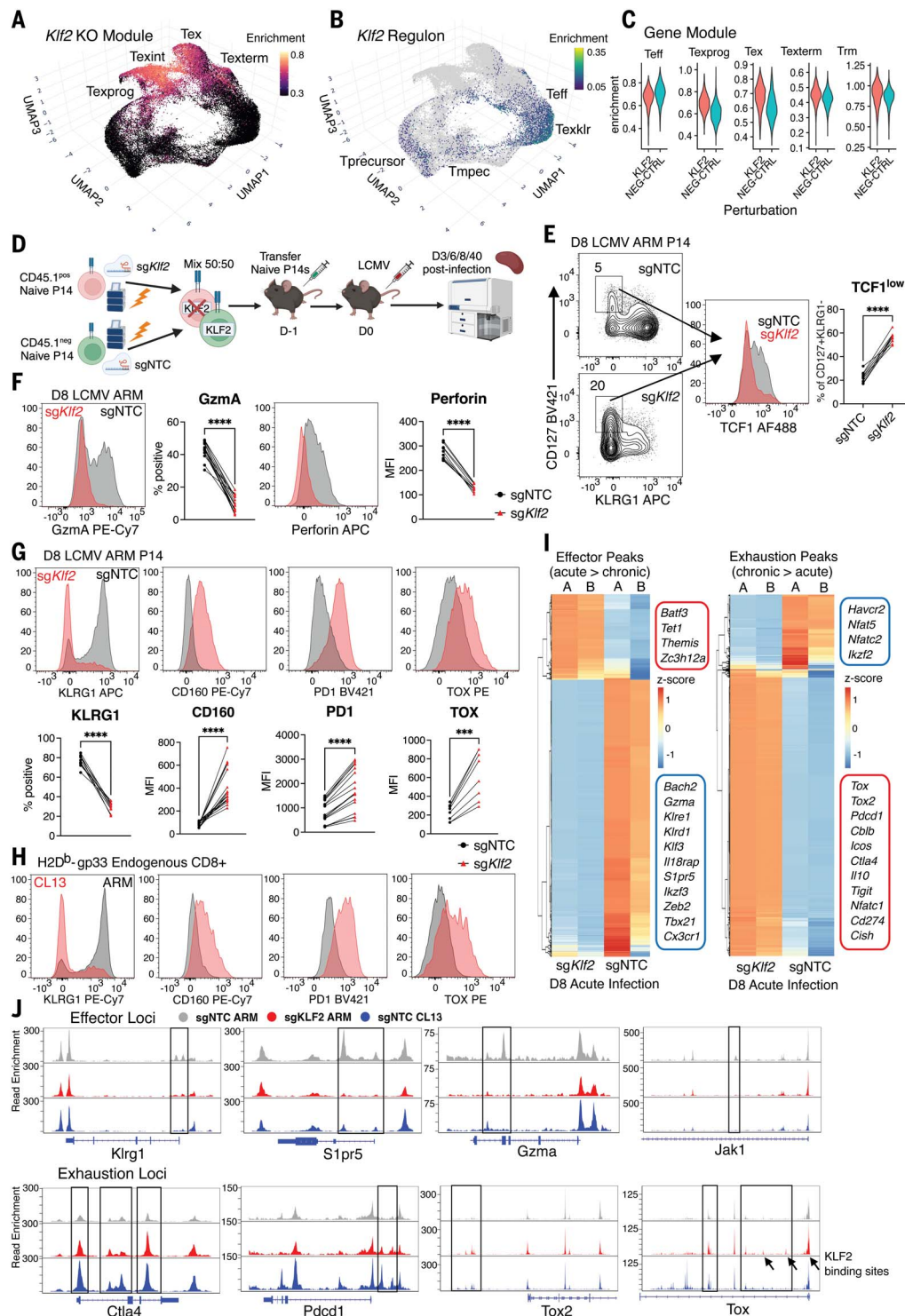
We then visualized how accessibility at these loci compared between KO and control cells from acute infection. KLF2 KOs had less and more accessibility at a majority of effector and exhaustion peaks, respectively (Fig. 3I). However, some loci did not follow this trend, suggesting they are regulated in a KLF2-independent manner (Fig. 3I, fig. S10C, and data S7 to S9). We also visualized the percent of differentially accessible peaks in the KOs that contained KLF2 binding sites (fig. S10D), determined by mapping to published chromatin immunoprecipitation sequencing data (*61*). This included KLF2 binding sites in the TOX locus, which had increased accessibility in the KOs (Fig. 3J). Furthermore, *Klf2* KOs had increased accessibility in the *Tnf* locus at sites of KLF2 binding, consistent with their increased potential to produce TNF-α (fig. S10E).

Unlike CD8 T cells in chronic infection, for which antigen is not cleared at day 8 (*62*), day 8 KLF2-deficient CD8 T cells in acute infection contained a substantial fraction of IL-7R^hi cells (Fig. 3E). IL-7R is a marker of Tmpec cells, but the absence of *Klf2* resulted in lower TCF1 expression in this population, a TF critical for memory cell formation (Fig. 3E). Analysis of the *Tcf7* locus also revealed KLF2 binding peaks and some differences in accessibility (fig. S10F). Moreover, the KLF2-deficient IL-7R^hi cells expressed exhaustion markers, such as CD160 (fig. S10G). Together, these data suggest KLF2 functions throughout the CD8 T cell effector and memory trajectory.

KLF2 KO exhaustion-like phenotypes emerge early in acute infection

As soon as day 8 of acute LCMV infection, the ratio of KLF2 KO to WT P14 cells had dropped from 50:50 to 25:75 (fig. S11A). To determine when differences arose between KO and WT, we transferred CellTraceViolet (CTV)–labeled naïve control and KO P14 cells into mice subsequently infected with acute LCMV (fig. S11B). At day 3 after infection, numbers and CTV dilution were similar between KLF2 KO and WT P14 cells, suggesting comparable proliferation in response to priming (fig. S11C). Yet, even at day 3, we observed up-regulation of exhaustion genes TOX, CD160, and CXCR6 in the KOs, pointing to their early differentiation toward an alternative fate (fig. S11D). At day 6 after infection, the KO and WT cells were still present at ~50:50 with the same phenotypic differences (fig. S11, A and E). To decipher whether this alternative fate decision was due to differences in antigen-sensing, we used P14 Nur77–green fluorescent protein (GFP) (*Nr4a1*) reporter T cells. KO P14s had lower Nur77-GFP reporter expression than their WT counterparts at day 6 (fig. S11F), suggesting that their exhaustion phenotype was not due to aberrantly high TCR signaling. Additionally, at day 8, a higher fraction of the KLF2 KOs were in the white pulp relative to control cells (fig. S12, A to C), but this was less pronounced at day 6 of infection (fig. S12A).

Differences in KO cell survival and differentiation could be associated with a change in responsiveness to cytokines that potentiate these, such as IL-15 and IL-2 (*8*). We observed that KO P14s from day 6 of LCMV infection had poor survival relative to their WT counterparts when cultured ex vivo in IL-15 but not in IL-2 (fig. S12D). Additionally, KLF2 KOs had reduced CD62L expression and increased CD69, CD25, CXCR6, and CXCR3 expression when cultured in IL-2 for 3 days after an initial 2-day activation, (fig. S13, A and B), suggesting enhanced responsiveness. We also observed an elevated response to type I IFN but saw no difference for transforming growth factor–β (TGF-β) or IL-12 (fig. S13C). These data suggest that an inability to respond to IL-2, IL-12, or type I IFN did not account for the phenotype or survival of the KLF2-deficient cells, but it may be explained by a reduced response to IL-15. The suddenness of the drop between days 6 and 8 could explain why this difference was not previously observed in experiments with acute *Listeria monocytogenes* infection (*63*). Alternatively, because CD8 T cells in chronic LCMV infection (and not acute) require antigen for persistence (*64*), clearance of antigen between days 6 and 8 could also contribute.

KLF2 suppresses TOX and enables TBET function, driving Teff differentiation

Given the increased chromatin accessibility at sites of KLF2 binding in the *Tox* locus, we hypothesized that KLF2 may repress TOX directly in a cell-intrinsic manner. We set up an in vitro assay to repeatedly stimulate control or KLF2 KO CD8 T cells with activation beads and observed an increase in TOX expression in the KO cells (Fig. 4A). We then performed rescue experiments to overexpress KLF2 in control and KO cells in acute infection (Fig. 4B and fig. S14, A and B). We observed strong repression of TOX, CD160, and PD-1 with KLF2 overexpression as well as induction of effector genes GzmA, Perforin, and KLRG1 (Fig. 4, C and D, and fig. S14C). Additionally, KLF2 overexpression in P14 T cells transferred into chronic infection resulted in reduced expression of PD-1 and TOX and a concomitant increase of effector proteins GzmB and KLRG1 (fig. S14D). These findings supported the idea that KLF2 directly suppresses T cell exhaustion in acute infection, in part through repression of TOX.

KLF2 was previously reported to promote Th1 over T follicular helper (Tfh) CD4 differentiation through induction of TBET (*65*). *Klf2* KO did not mirror *Tbx21* KO in our perturbSEQ, but prior work has demonstrated that TBET is necessary and sufficient for the development of Teff cells in acute and chronic infection (*8*, *25*). Thus, we hypothesized that the absence of Teff differentiation in KLF2 KOs could be due to TBET. We saw decreased TBET protein and *Tbx21* mRNA in the KLF2 KO cells at day 8 of acute infection (Fig. 4E). However, even when gating on a normalized intermediate level of TBET, we observed a reduction in KLRG1 expression (fig. S14E). Further, motif enrichment analysis revealed reduced accessibility of TBET binding motifs in the KLF2 KO cells (Fig. 4F), leading us to hypothesize that the presence of KLF2 was critical for the function of TBET in driving Teff differentiation. To test this, we performed epistasis experiments by overexpressing TBET in WT and KLF2 KO P14 T cells in acute infection (fig. S14F). TBET overexpression augmented KLRG1 and GzmA in WT P14 CD8 T cells but failed to restore effector differentiation in KLF2 KO cells fully (Fig. 4G). Additionally, TBET overexpression did not suppress TOX, CD160, or PD-1 in the KOs (fig. S14G).

The lack of TBET function in KLF2 KO cells could alternatively be explained by an inability to reach an adequately high expression threshold in our assay, as the highest level of mCherry expression (reporter for TBET overexpression) induced the greatest expression of KLRG1 (fig. S14H). TBET overexpression in KOs did not reach the protein levels seen with overexpression in WT cells (fig. S14I), but, by normalizing for intermediate mCherry and TBET expression, we still found that KOs had a substantial deficit in inducing effector differentiation (fig. S14J).

KLF2 is dispensable for memory but is required for functional memory recall

KLF2-deficient IL-7R^hi Tmpec had several apparent deficiencies that might preclude memory formation, including lower expression of TCF1, reduced survival in IL-15, and expression of markers associated with exhaustion. Thus, we asked whether KLF2 was required for memory CD8 T cell development after infection. KLF2 KO and WT P14 T cells were mixed 1:1 and transferred into mice that were infected with acute LCMV (Fig. 5A and fig. S15A). Between days 8 and 40 after infection, we observed an increase in the relative fraction of KO versus WT cells in the spleen (Fig. 5, B and C). Moreover, KLF2 KO cells exhibited phenotypic features of memory and tissue residence, specifically IL-7R and P2RX7 (*66*, *67*), whereas maintaining TOX and CD160 expression (Fig. 5, D and E, and fig. S15B). In contrast to day 8, KO CD127^+ memory cells had high TCF1 expression (fig. S15C) in line with some reported plasticity at this locus (*68*). KOs expressed lower levels of the cytolytic molecules GzmA and Perforin1 relative to WTs, but retained some potential to produce IFN-γ and TNF-α upon ex vivo restimulation (fig. S15, D and E).

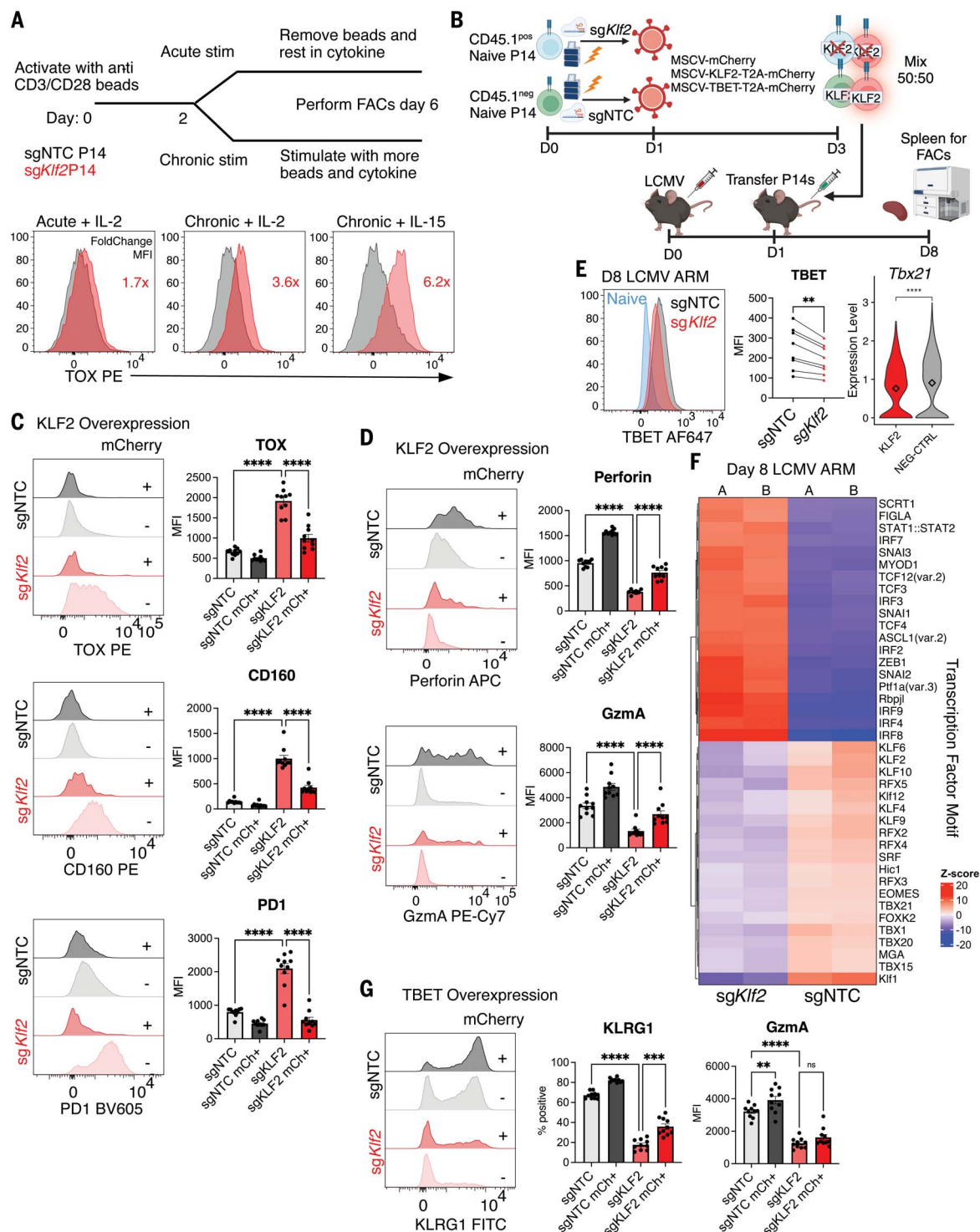A hallmark of T cell memory is its ability to robustly expand and differentiate into effector

Fig. 4. KLF2 suppresses TOX and supports the function of TBET in acute LCMV infection. (**A**) Control and KLF2 KO P14s were acutely or chronically stimulated with activation beads in vitro; representative flow plots showing increased induction of TOX in KO cells. Data is representative of three independent experiments. (**B**) Schematic of KO and overexpression workflow; KOs were generated as in Fig. 3D and were then transduced prior to 50:50 mixing and transfer into day 1 LCMV ARM–infected mice. (mCherry identifies transduced cells). (**C**) Flow analysis demonstrating KLF2 over-expression in control and KO P14s leads to suppression of exhaustion protein expression. N = 10 mice replicates, representative of two independent

experiments. (**D**) KLF2 overexpression activates functional effector protein expression. N = 10 mice replicates, representative of two independent experiments. (**E**) Representative flow plot highlights slightly reduced TBET mean fluorescence intensity (MFI) in KLF2 KOs; a slight reduction is seen at the RNA level as well (data from perturbSEQ). N = 8 mice replicates, representative of two independent experiments. (**F**) Motif accessibility analysis from ATAC-seq demonstrates a reduction in KLF family and TBET motif accessibility in KOs as well as an increase in IRF family accessibility. (**G**) TBET overexpression in KLF2 KO P14s fails to induce effector protein expression relative to WT counterparts. N = 10 mice replicates, representative of two independent

experiments. All flow plots were pregated on live P14s, representative gating schemes shown in figs. S8A and S14A. Mean ± SEM is shown for all bar plots, Wilcoxon rank sum test (*Tbx21* RNA), paired *t* test (TBET MFI), and paired ANOVA [(C), (D), and (G)] were used to find statistical significance; **$P < 0.01$; ***$P < 0.001$; ****$P < 0.0001$. Individual data points each represent one mouse, with the connecting line indicating paired samples as KO and WT cotransfers were performed.

cells upon rechallenge (*69*). To test this, we harvested day 40 KO and WT memory cells and transferred into naïve recipients, which were subsequently infected with acute LCMV (Fig. 5A). KLF2 KO memory T cells mounted a deficient recall response on day 6 (Fig. 5, B and F) and underwent aberrant differentiation at the expense of a functional effector fate (Fig. 5, G and H, and fig. S15F). Notably, KO cells retained the ability to make cytokines despite two rounds of exposure to acute infection (Fig. 5I). Given the ability of the recipient mice to clear infection, this could reflect a lack of sufficient exposure to chronic antigen to drive cytokine loss and suggests that factors other than KLF2 control this aspect of the exhausted cell state. Our findings were reminiscent of what has been shown in prior work where Tex cells from chronic infection were transferred into uninfected recipients and rechallenged (*60*). Thus, KLF2 was dispensable for the long-term survival of CD8 T cells after acute infection but was critical for their ability to recall and differentiate into Teff cells in the secondary response.

KLF2 maintains progenitor-exhausted TPEX1 cells and suppresses tumor-specific CD8 T cell exhaustion

KLF2 is regulated by TCR stimulation and many cytokines, including the γ-chain cytokines, IL-12, type I IFNs, and TGF-β. (*70–73*). We hypothesized that TCR-mediated downregulation of KLF2 is crucial for an early fate decision to enter an exhausted trajectory. We observed decreased expression of *Klf2* as cells traveled along the exhausted trajectory in chronic infection, with apparent silencing of *Klf2* at the most extreme points of the Tex and Texterm populations (Fig. 6A and fig. S16A). Additionally, stimulation of naïve CD8 T cells with increasing amounts of activation beads resulted in a dose-dependent decrease in KLF2 protein (Fig. 6B). This suggested the natural course of exhaustion involves KLF2 downregulation at the point when effector and exhaustion trajectories split.

Recent work has further dissected these early T cell fate decisions in chronic antigen settings with a particular emphasis on progenitor-exhausted (TPEX) cell states (stem-like or exhausted progenitors). This work highlighted the progressive differentiation of CD8s from a MYB⁺ CD62L⁺ TPEX1 cell to a MYB⁻ CD62L⁻ TPEX2 cell, of which MYB was a key regulator (*74*). Reanalysis of data from of T cells isolated from KP-NINJA (neoantigen-expressing *Kras*[G12D] *p53*[null]) autochthonous lung tumors and draining lymph nodes previously published by our lab

(*42*) showed that these CD62L⁺ cells were not fully committed to the exhaustion lineage and retained canonical memory traits at the epigenetic level. This correlated with the cells having superior antitumor efficacy and potential to respond to immunotherapy (*75*). Moreover, *Klf2* was differentially expressed between TPEX1 and TPEX2 and was lower in the TPEX2 cells (*75*). We also observed increased accessibility at the Myb locus in KO cells, specifically at sites of KLF2 binding (fig. S16B). Our LCMV DSM Texprog population did not have sufficient resolution to identify TPEX1 and TPEX2 populations, but we confirmed the KP-NINJA finding in our own reanalysis (Fig. 6, C and D, fig. S16C, and data S10) and therefore reasoned that the tumor-draining lymph node (tdLN) would be a tractable system for testing the role of KLF2 in the TPEX1 to TPEX2 differentiation step.

As in chronic LCMV (*74*), the TPEX1 population in the tdLN expressed *Tcf7*, *Tox*, *Id3*, *Slamf6*, and *Sell* (*CD62L*) as well as high levels of the TF *Myb* (Fig. 6E). Notably, *Klf2* expression was far more restricted to TPEX1 than *Tcf7*, which was more broadly expressed in both TPEX1 and TPEX2 populations (Fig. 6D and fig. S16D). The TPEX1 and TPEX2 subsets were not observed in the tumor, where instead *Cxcr6*-expressing Texterm cells were primarily found (fig. S16, D and E). Critically, *Klf2* was expressed in the naïve (1) and TPEX1 (0) clusters in the tdLN but was downregulated in the TPEX2 (3) and Texterm (2) clusters (Fig. 6D). Conversely, the KLF2 KO gene module (perturbSEQ) was upregulated in TPEX2 (3) and Texterm (2) clusters (fig. S16D). At week 8, there were small early-activated (6) and effector-like (5) clusters in the tumor that also expressed KLF2, but these were absent from the tumor at week 17. Additionally, there was a concomitant shift from TPEX1 to TPEX2 in the tdLN at week 17 (fig. S16C). Together, these data suggested that the transition between TPEX1 to TPEX2 was the point at which KLF2 was downregulated, enabling entry to the exhaustion program.

We generated KO P14 T cells and transferred them into KPN1.1 (gp33⁺ KP lung tumor cell line) tumor-bearing *Tcra* KO mice, allowing us to isolate the antitumor response to transferred T cells only (Fig. 6F) (*76*). Mice that received KLF2 KO cells experienced faster tumor growth relative to those that received WT cells (Fig. 6G). The KLF2 KO cells in the tdLN had decreased TCF1 expression (Fig. 6H and fig. S16F), and there was a loss of CD62L⁺ TPEX1 cells in favor of a CXCR6⁺ differentiated state (Fig. 6I). Notably, *Cxcr6* was naturally expressed by cells in the KP-NINJA

tumors with far less expression in the tdLN (Fig. 6E and fig. S16E), suggesting aberrant differentiation in the tdLN in the absence of KLF2. This CXCR6⁺ state is also potentially reflective of tdLN tissue resident cells defined previously (*77*). In line with this increased differentiation, a higher fraction of KO cells in the tumor were TCF1^{low} and had PD-1 and TIM3 coexpression (Fig. 6J and fig. S16G).

These data suggested that KLF2 was required to maintain the TPEX1 state and avoid differentiation to a Texterm state. To test whether KLF2 expression was sufficient, we devised an inducible estrogen receptor (ER)–KLF2 fusion construct so that we could sequester KLF2 in the cytoplasm prior to exposure of cells to tamoxifen, whereby KLF2 would be shuttled to the nucleus to perform its function (fig. S16, H and I). We transduced congenically distinct KLF2 KO and WT P14 T cells, mixed them 50:50, and transferred them into day 7 KPN1.1 tumor-bearing B6 mice. Mice were subsequently treated with tamoxifen through diet and gavage for 3 weeks while tumors grew (Fig. 6K). We harvested tdLNs at day 28 after the tumor injection and observed that KLF2 overexpression had rescued the CD62L⁺ CXCR6⁻ TPEX1 cells in the KO and WT CD8 T cells (Fig. 6L). Together, these data supported the role of KLF2 in maintaining a progenitor state and suppressing the exhaustion program.

Discussion

Naïve CD8 T cells have the potential to differentiate into diverse effector and memory cell states. These states are endowed with distinct functional properties, such as self-renewal (memory), cytolytic potential (effector), or persistence in the face of chronic antigen (exhausted). Exhaustion is a T cell state thought to be induced in the context of chronic antigen exposure and is correlated with the expression of numerous coinhibitory receptors and reduced functional potential, including proliferative capacity and cytokine production (*22*). TFs and EMs may influence differentiation in at least two ways: (i) alteration of the extent to which cells differentiate along a specific trajectory or (ii) suppression or promotion of differentiation toward alternative fates. Most TFs and EMs examined in our study modulated the extent to which CD8 T cells differentiated along a defined and expected linear effector trajectory. Unexpectedly, KLF2 suppressed exhaustion-related gene expression, facilitating TBET function and maintaining effector lineage fidelity during acute LCMV infection. KLF2's role was further elucidated in tdLNs, where it was necessary and sufficient to maintain a TPEX1
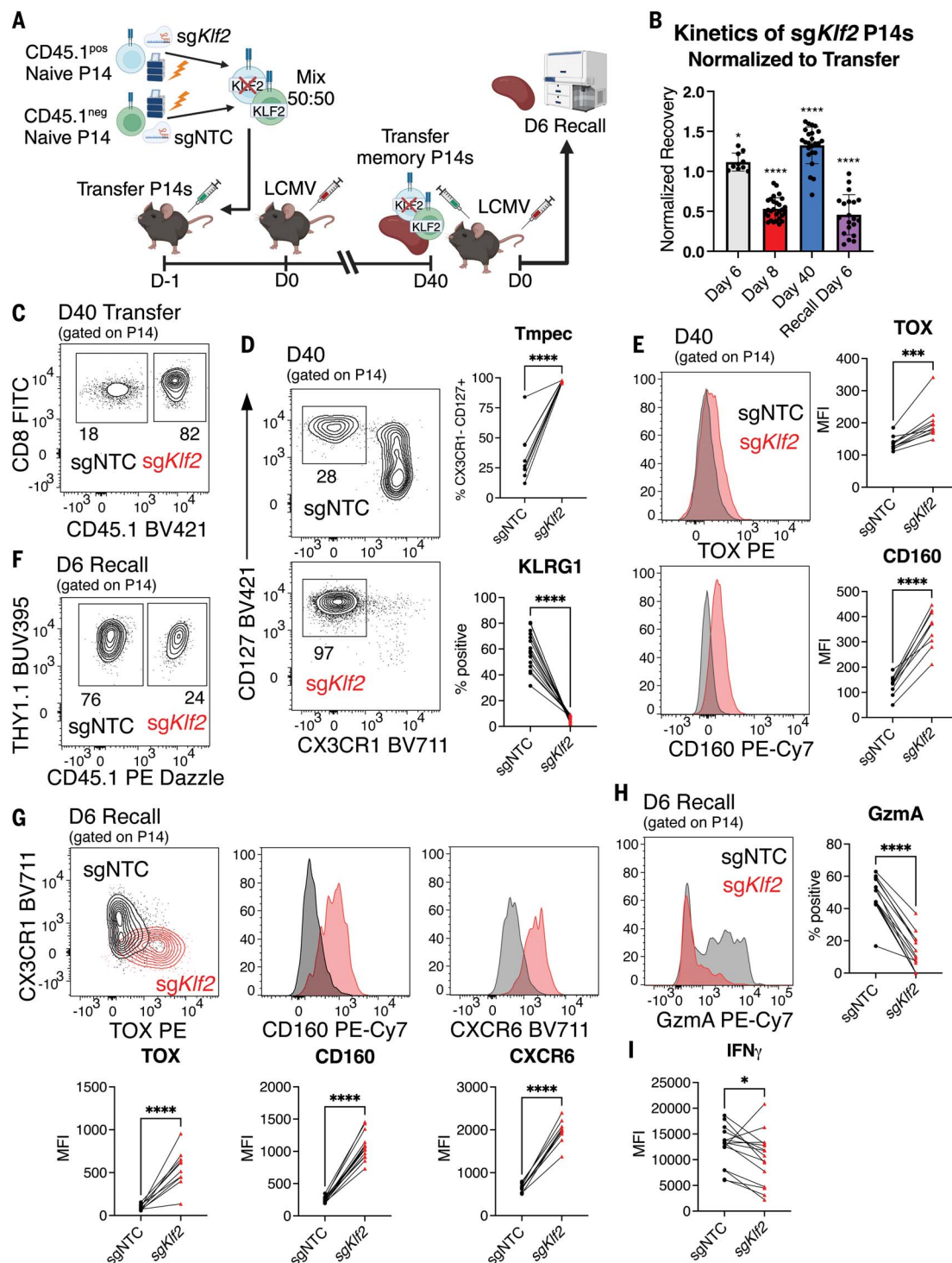
Fig. 5. KLF2 is required for functional memory recall. (**A**) Experimental schematic used to generate memory KO and WT P14 T cells and test recall potential in LCMV ARM infection. (**B**) Kinetics of KLF2 KO P14s over the course of primary infection and secondary rechallenge; each time point is normalized to relevant transfer. Mean ± SD is shown on the bar plot. N = 10 to 28 mice replicates, combined data from three to four independent experiments based on time points. (**C**) Representative flow plot of KLF2 KO and control P14s at time of day 40 (D40) memory transfer. (**D** and **E**) Phenotype of knockouts and control P14s from spleen at day 40 after LCMV ARM infection. N = 10 mice replicates, representative of three independent experiments. (**F**) Representative flow plot of ratio of control to KO P14s at day 6 of recall response after memory transfer and LCMV ARM rechallenge. (**G**) Flow analysis demonstrating

strong induction of exhaustion protein expression at the expense of effector differentiation in KLF2 KOs during recall response; P14s from day 6 PI spleen. N = 10 to 15 mice replicates, combined or representative data of three independent experiments. (**H**) GzmA production after ex vivo gp33 stimulation; control and KOs isolated from spleen at day 6 recall. N = 15 mice replicates, combined data from three independent experiments. (**I**) IFN-γ production on per-cell basis (MFI) of KO and WT P14s at day 6 recall. N = 15 mice replicates, combined data from three independent experiments. All flow plots were pregated on live P14s; the gating scheme is shown in fig. S15. A paired t test was used to find statistical significance for all flow data;*P < 0.05; ***P < 0.001; ****P < 0.0001. Individual data points each represent one mouse, with the connecting line indicating paired samples as KO and WT cotransfers were performed.
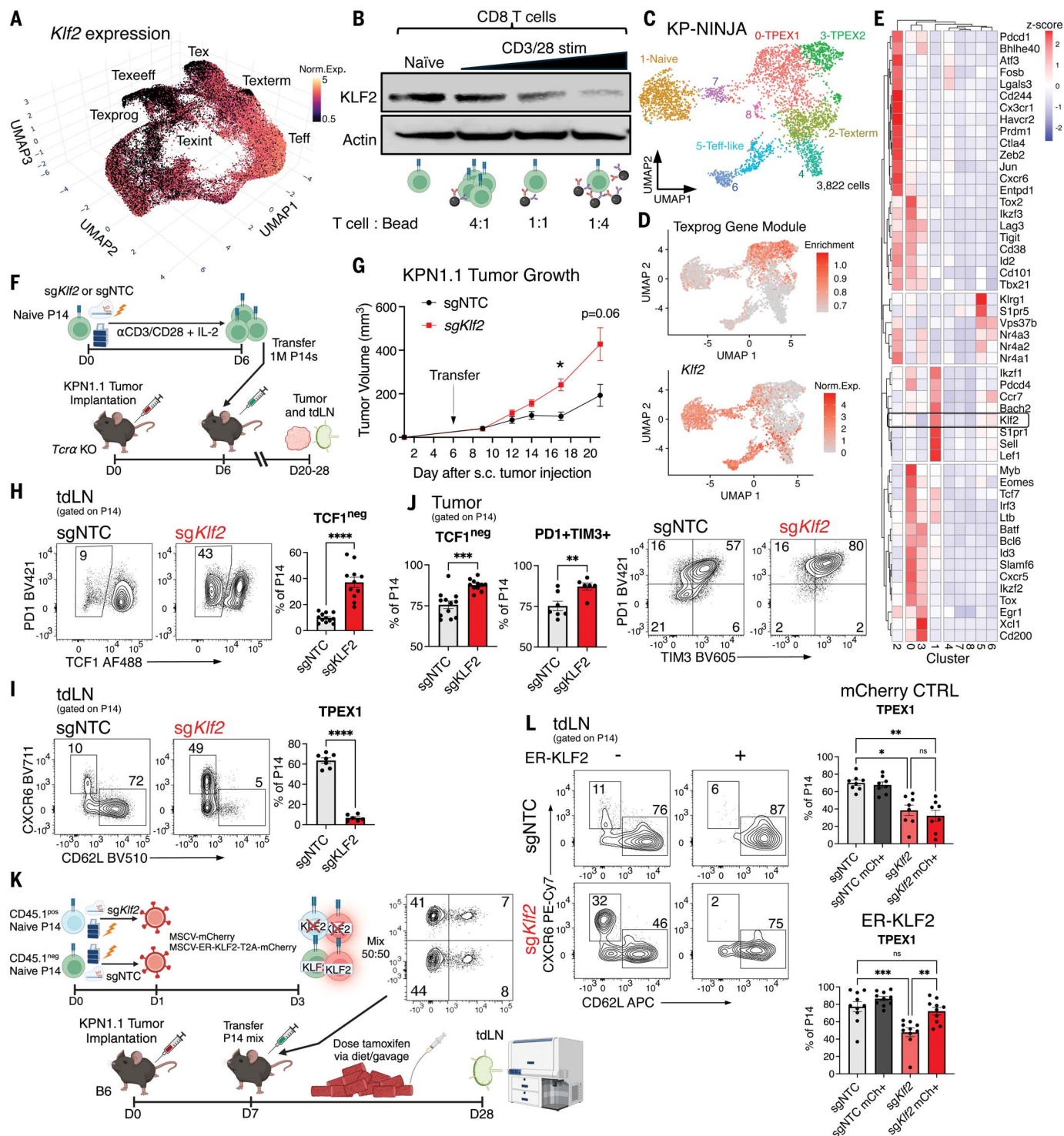
Fig. 6. KLF2 maintains TPEX1 cells and suppresses tumor-specific T cell exhaustion. (**A**) RNA expression of *Klf2* on map of LCMV differentiation states; the lowest expression is seen on the exhaustion trajectory. (**B**) Naïve CD8 T cells were stimulated for 24 hours with increasing amounts of activation beads; a western blot was performed for KLF2, showing TCR dependent down-regulation. Data is representative of two independent experiments. (**C**) gp-33–specific CD8 T cells were sorted out of KP-NINJA tumor-bearing lungs and draining lymph nodes (tdLNs) at early (week 8) and late (week 17) time points to perform scRNA-seq; UMAP reduction and clustering reveals distinct differentiation states (*42*). (**D**) Gene module enrichment highlights TPEX1 and TPEX2 clusters with

strong Texprog (LCMV) signature enrichment; *Klf2* expression was seen in naïve, TPEX1, and Teff-like clusters. (**E**) Heatmap showing canonical gene expression across clusters; *Klf2* and *Myb* was expressed in TPEX1 cells. (**F**) Experimental schematic; control and KO P14s were generated by Cas9 RNP electroporation and then activated and expanded prior to transfer into tumor-bearing T-cell–deficient recipients. (**G**) Tumor growth curves of KPN1.1 tumor-bearing mice receiving control or KLF2 KO P14s. *N* = 11 mice replicates per condition, representative of three independent experiments. (**H**) Expression of TCF1 and PD-1 in the tdLN; TCF1⁺ are TPEX. *N* = 11 to 12 mice replicates per condition, representative of three independent experiments. (**I**) Expression of CD62L and

CXCR6 in tdLN; CD62L⁺ are TPEX1. *N* = 6 to 7 mice replicates per condition, representative of two independent experiments. (**J**) TCF1 expression and PD-1 and TIM3 coexpression of control and KO P14s from tumors. *N* = 11 to 12 (TCF1) or 6 to 7 (TIM3) mice replicates per condition, representative of three independent experiments. (**K**) Experimental schematic; KLF2 KO and control P14s were transduced with an inducible ER-KLF2 vector, mixed, and transferred into KPN1.1 tumor-bearing B6 mice; mice were then administered tamoxifen by diet and gavage. (**L**) Inducible

KLF2 activity drove TPEX1 maintenance in KO and control P14s in the tdLN as shown by CD62L⁺ CXCR6⁻ population. *N* = 10 mice replicates, representative of two independent experiments. All flow plots pregated on live P14s; gating scheme shown in fig. S16A; Mean ± SEM shown for all plots, unpaired *t* tests were used to find statistical significance of tumor growth and panels (H) to (J), and paired ANOVA was used for panel (L). *$P < 0.05$;**$P < 0.01$; ***$P < 0.001$; ****$P < 0.0001$. Individual data points each represent one mouse, and data points across conditions are paired in (L).

state. These studies underscore the complex function of KLF2 as a molecular guardrail preventing aberrant CD8 T cell differentiation.

Our study supports a linear effector CD8 differentiation model in acute infection. Although previous work has demonstrated the utility of cell state–specific markers, these definitions often grant uncertainty to whether the effector CD8 T cell pool comprises discrete subsets or whether the potential is on a continuous gradient (*49*). Our perturbSEQ analyses suggested at least three main, discrete populations. Several gene KOs were notable because they did not appear to progress beyond a certain point, suggesting that their activity is required for forming a respective cellular state along the linear effector trajectory. Yet, no KOs were in exclusively one population, which could be explained by technical limitations of the assay (e.g., incomplete KO efficiency), a biological limitation of the process, or redundancy between factors. Additionally, a TF or EM required to exclusively trap cells in one state may not have been targeted within our perturbSEQ pool.

Previous work has shown that KLF2 is highly expressed in effector T cells during acute LCMV infection and differentially expressed between Texklr and Texterm from chronic LCMV infection (*16*, *18*, *26*, *59*, *78–80*). Additionally, KLF motif accessibility decreases as cells differentiate toward exhaustion in tumors (*80*). However, the role of KLF2 in dictating effector and exhaustion states remained uncertain, as most studies focused on its function in migration or TRM formation (*63*, *81–83*). Although we cannot rule out that KLF2 alters the position of cells within a tissue to drive its effect, our data are consistent with a position-independent role for KLF2. One recent study showed that KLF2 deficiency in CAR-T cells shifts the balance of effector to exhausted cells with the implication that KLF2's main function in this process is suppression of *Tox* (*61*). This finding is at odds with data showing *Klf2* was down-regulated between TPEX1 and TPEX2 cells, which do not differ in *Tox* expression (*74*). Moreover, in the context of chronic infection and cancer, many TFs, including BATF, BLIMP1, TBET, TCF1, TOX, and KLF2, have been suggested to regulate the exhausted versus effector fate decision (*25*, *59*, *61*, *84–86*), yet KLF2 specifically had this role in acute infection, enabling us to clarify mechanisms related to its function in this process. Our findings suggest that KLF2

loss can initiate this fate decision independent of a distinct set of signals in chronic antigen challenge such as repeated or prolonged TCR stimulation. Combining our findings in infection and tdLNs, we hypothesize that the transition between TPEX1 and TPEX2 states is a point of bifurcation for the exhaustion and effector trajectories and where KLF2 elicits its physiological function. We and others observed that TCR signals can lead to downregulation of KLF2 and may facilitate this early fate decision. ATAC-seq analyses revealed an increase in IRF and STAT1 motif accessibility in the KLF2 KOs, suggesting a potential role for type I IFNs in our findings and in physiological conditions of KLF2 down-regulation. Thus, our data are consistent with a model where the repeated exposure to TCR signals and inflammatory cytokines during chronic infection and cancer leads to suppression of KLF2, thereby allowing differentiation toward an exhausted cell state.

Our analyses of DEGs and differentially accessible peaks between KOs and cells from chronic infection highlighted features of the exhaustion program that are likely regulated by KLF2 and those that are independent. It is therefore implied that further signals, such as those mentioned above, are still required for cells to commit to a terminally exhausted state, resulting in loss of the production of cytokines, such as TNF-α (*33*, *87*), as we did not see this with KLF2 KO alone. This was demonstrated by studies showing that day 8 chronic infection CD8 T cells have a "reversible" phenotype if they are transferred into an antigen-free environment (REC-Tex) (*26*, *88*), whereas day 15 cells do not, as they shift from "exhausted-precursor" to "progenitor-exhausted" cells (*26*). Removal from antigen is a requisite to form memory, and we found that KLF2 KO CD8 T cells were able to form long-lived memory that had properties associated with REC-Tex cells from chronic infection (*60*). Thus, we hypothesize that *Klf2* loss or down-regulation opens the door to the exhaustion lineage, but additional signals are still required before the cells fully commit to a terminally exhausted state.

Materials and methods
Study design

The aim of this study was to investigate CD8 T cell fate decisions and specifically the transcriptional and epigenetic regulators underly-

ing them. We used mouse models of acute and chronic infection to generate a map of possible CD8 T cell differentiation states. We then performed pooled single-cell CRISPR screening to understand the role of ~40 TFs, epigenetic modulators, and cell-to-cell interaction genes in regulating CD8 T cell differentiation in acute infection. The genes targeted in this study were informed from our map and prior literature. We then used Cas9 RNP editing of naïve CD8 T cells to primarily validate the role of KLF2 and mechanistically understand its regulatory function. This included flow cytometry of cells from acute infection and tumor models as well as ATAC-seq to understand epigenetic changes happening under KLF2 control. We overexpressed KLF2 in acute and chronic infection to further elucidate its function and performed TBET epistasis experiments to this end. In conjunction with these experiments, we performed various in vitro assays to test the ability of KLF2 KOs to respond to several stimuli in a controlled manner. Lastly, we reanalyzed a KP-NINJA lung tumor dataset produced in our lab previously to investigate KLF2's early regulation of the T cell exhaustion fate decision. Further, Cas9 RNP KO and overexpression studies in our tumor model directly assessed KLF2's function in this context.

Mice

Animal care and procedures were conducted in accordance with approved methods by the Institutional Animal Care and Use Committee of Yale University. C57BL/6J (B6) mice were purchased from JAX (stock no. 000664) and bred in house. THY1.1⁺ dsRED-expressing TCR transgenic P14 mice were generated in house by crossing THY1.1⁺ P14 mice (*89*) to dsRED-expressing mice (JAX, stock no. 006051). Other P14 mice were bred in house by crossing with Ly5.1 mice from JAX (stock no. 002014). P14 dsRED mice were crossed to H11^Cas9 mice from JAX (stock no. 028239) to generate P14 dsRED H11^Cas9/wt mice used in perturbSeq (*90*). H11^Cas9 were crossed to B6 to generate H11^Cas9 heterozygous recipient mice. *Tcra* KO mice were purchased from JAX (stock no. 002116). Mice were housed (five per cage) in a controlled environment with free access to food/water and enrichment nestlets. There was a fixed 12-hour light cycle at an ambient temperature of ~23°C. Both male and female mice were used in studies aged 6 to 12 weeks and were sex- and age-matched and randomized to receive either KO

or control cells when cotransfers were not performed. Tamoxifen diet was used in experiments with ER-KLF2 transduced cells and was given to mice in pellet form (Teklad TD.130856). No other special diets or water were used. Euthanasia was performed through isoflurane overdose followed by cervical dislocation. Investigators were not blinded during experimental procedures or outcome assessments.

For genotyping, mouse ear DNA was amplified using GoTaq G2 Green Master Mix (Promega, M7823) or KAPA Taq PCR Kit (Takara Bio, R040A).

Mouse infection and tumor models

B6 mice were infected with LCMV Armstrong at 2×10^5 plaque-forming units (pfu) per mouse intraperitoneally or LCMV clone 13 at 4×10^6 pfu (2×10^6 pfu in KLF2 overexpression study) per mouse intravenously. Mice were euthanized 4, 6, 8, 28, or 40 days after infection to collect spleens. Both LCMV Armstrong and LCMV clone 13 were produced in house. Pilot studies were performed to determine mouse number required to recover sufficient cells post-harvest and sort for relevant studies.

KPN1.1 cell line was generated in house and derived from KP-NINJA lung tumor which was then passaged subcutaneously through a B6 recipient; 500,000 to 1 million cells were injected subcutaneously for experiments. For inducible ER-KLF2 experiments, tumor bearing mice were given oral gavage of 200 µg of tamoxifen in corn oil for three doses and then given tamoxifen diet until study completion (see details above).

PerturbSeq library design and molecular biology

sgRNAs for each target gene were selected by CHOP CHOP (data S2) (91). The retroviral vector was constructed through Gibson assembly by using gene blocks (IDT) and a MSCV backbone. sgRNAs were cloned into this vector in an arrayed fashion by annealing complimentary oligos encoding the sgRNAs and inserting into the sgRNA cassette by restriction cloning. Each sgRNA's successful insertion was validated by Sanger sequencing before pooling all cloned sgRNAs together at equal molar ratios. The exception to this was the six non-targeting control sgRNAs which were each added in to represent 2.5% of the library each for a total of 15%. This pooled MSCV sgRNA library was transfected into Platinum-E (Cell Biolabs RV-101) cells to produce retrovirus used for downstream workflows. Overexpression vectors were cloned and used to generate retrovirus in the same fashion via Gibson assembly of gene blocks encoding codon optimized cDNA and mCherry reporter under an EF1α promoter on a MSCV backbone. Note KLF2 cDNA was mutated at sgRNA cut sites to prevent cutting of overexpression sequence. Retroviral constructs for overexpression of KLF2

in chronic infection were constructed by replacing GFP with Thy1.1 in the common MIG vector prior to insertion of codon optimized KLF2.

T cell transduction

P14 DsRED Cas9 T cells were isolated from spleen the EasySep CD8 T cell negative selection kit (STEMCELL Technologies, 19853) according to the manufacturer's instructions. T cells were then activated with anti-CD3/CD28 Dynabeads (ThermoFisher Scientific, 11452D) at a 1:1 ratio in the presence of recombinant human IL-2 at 5 ng/mL (Peprotech 200-02). On day 1 of activation, T cells were spinfected with retroviral supernatant in the presence of protamine sulfate (5 µg/mL) at 600g for 90 min. Two days after transduction, T cells were positively selected for human CD2 with the EasySep Human CD2 positive selection kit (STEMCELL 17883). The following day, positively selected P14 DsRED Cas9 T cells were transferred into congenic recipient mice who were infected with acute LCMV 1 day prior. P14 T cells were transduced in the same fashion with overexpression vectors but were transferred without positive selection for mCherry/Thy1.1 reporter. For LCMV experiments, 50,000 to 100,000 P14s were transferred; for tumor experiments, 500,000 to 1 million P14s were transferred.

Western blot

T cells were pelleted and resuspended in 1X RIPA buffer (from 10X concentrate; Millipore 20-188) containing PhosSTOP phosphatase inhibitors (Roche 4906845001) and complete protease inhibitors (Roche 11836153001) and passed through a QIAshredder column (QIAGEN 79656). Protein concentration was determined (BioRad 5000111) and normalized across samples with 20 µg protein per sample loaded. After transfer, membranes were probed with polyclonal anti-KLF2 immunoglobulin G (IgG) (1:500; LS Bio LS-B5627-50), polyclonal horseradish peroxidase (HRP)–conjugated antirabbit IgG (Cell Signaling Technology 7074) and developed with SuperSignal West Femto Maximum Sensitivity Substrate (ThermoFisher Scientific 34096). HRP-conjugated anti–β-actin (1:2000; C4 clone; Santa Cruz Biotechnology sc-47778) was used as a loading control. All antibodies were diluted in 5% nonfat milk in TBS containing 0.5% Tween-20.

Naïve T cell CRISPR

Naïve P14 CD8 T cells were isolated from spleen using the EasySep CD8 T cell negative selection kit (STEMCELL Technologies, 19853) according to the manufacturer's instructions. The gene-editing protocol was adapted from (92). In brief, Cas9-sgRNA ribonucleoproteins were formed by mixing sgRNA (CRISPRevolution sgRNA EZ Kit, Synthego) with Cas9 nuclease V3 (IDT, 1081059). In total, 2×10^6 to 5×10^6

P14 CD8 T cells were mixed with Cas9–sgRNA ribonucleoproteins and electroporated with the Lonza P3 Primary Cell 4D-Nucleofector X kit (V4XP-3032) according to the manufacturer's instructions. In the case of in vivo LCMV experiments, control and experimental cells were then mixed 1:1 and immediately transferred into recipient mice via retroorbital injection; 10,000 cells per mouse unless otherwise noted. Nontargeting control sgRNAs (sgNTCs) were use as negative controls for all experiments. For in vitro experiments, cells were then activated with anti-CD3 and anti-CD28 Dynabeads (ThermoFisher Scientific, 11452D) for downstream workflows. For the memory recall experiment, day 40 postinfection P14 CD8 T cells were positively selected out of the spleen using the CD90.1 positive selection kit (STEMCELL Technologies, 18958) prior to their transfer via retroorbital injection into naïve recipient mice. This transfer was therefore reflective of the cell ratio at day 40 ~80:20 KO:WT. Those mice were then infected 1 day later. Owing to the expression of P2RX7 at day 40, we also injected mice with "Treg protector" nanobody (Biolegend 149803) 20 min prior to sacrifice to exclude cell death as a variable impacting our findings. KO memory recovery and recall capability was similar with or without this injection and all data was combined for presentation and statistics. All sgRNA sequences used in validation studies are highlighted in data S10.

In vitro stimulations

Naïve P14 CD8 T cells were isolated and edited with sgRNA as above. For cytokine stimulations, cells were then activated with anti-CD3/CD28 Dynabeads (ThermoFisher Scientific, 11452D) for 48 hours. Activated cells were plated at 100,000 cells per well in a 96-well plate and stimulated with 10, 1, 0.1, or 0.01 ng/mL of IL-2 (PeproTech, 200-02), IL-12 (R&D Systems, 419-ML-010), IL-15 (PeproTech, 210-15), IFN-β (R&D Systems, 8234-MB-010), IL-12 (R&D Systems, 419-ML), or TGF-β (R&D Systems, 7666-MB-005) for 48 hours. For chronic stimulation, edited P14 cells were cultured in 1 ng/mL of IL-2 (PeproTech, 200-02) or IL-15 (PeproTech, 210-15) and activated with anti-CD3 and anti-CD28 Dynabeads (ThermoFisher Scientific, 11452D) at a 1:1 ratio of beads to cells. At day 2, "acutely" activated cells were removed from beads and cultured in cytokines alone, whereas "chronically" activated cells were maintained on Dynabeads plus cytokines through day 6. Cells were collected and directly stained for flow cytometry as below.

Tissue processing for flow cytometry

For intravenous labeling experiments, mice were injected retro-orbitally with 200 µL of anti-CD45 BUV661 antibody prior to euthanasia. After 5 min, spleens were harvested from

mice for downstream analysis. Spleens were smashed through 70-μM filters and processed in FACS buffer (2% HI FBS, 1mM EDTA in 1x PBS without Mg^{2+}/Ca^{2+}). Red blood lysis was performed using 1X RBC lysis buffer (eBioscience 00-4333-57). Resulting cells were then used for downstream stimulations or direct flow cytometry staining. Lymph nodes were processed in the same fashion without RBC lysis. Tumors were harvested into Collagenase IV (Worthington Biochemical, catalog LS004189) buffer [1× Hepes buffer, Collagenase IV (0.5 mg/ml), and deoxyribonuclease (20 μg/ml) in 1× Hanks' balanced salt solution with $MgCl_2$ and $CaCl_2$] and manually chopped up prior to incubation at 37°C for 30 to 40 min. Digestion was quenched by adding 500 μl of FBS and samples were then filtered.

Ex vivo cytokine expression

Single-cell suspensions were obtained as described above. Splenocytes were then plated in 96-well plates and stimulated in 10% HI-FBS RPMI-1640 (Thermo Fisher Scientific, catalog 11875085) containing Brefeldin A (eBioscience, catalog 00-4506-51), Monensin (BD catalog 51-2092KZ), and LCMV GP_{33-41} peptide (AnaSpec, catalog AS-61296) or left unstimulated in 10% HI-FBS RPMI-1640 (Thermo Fisher Scientific, catalog 11875085) containing Brefeldin A (eBioscience, catalog 00-4506-51) and Monensin (BD catalog 51-2092KZ). Antibody against CD107a was added to the culture as well. Plates were incubated for 5-6 hours at 37° and then spun down. Samples were stained for extracellular markers (see the "Flow cytometry" section), fixed with the BD Cytofix/Cytoperm Fixation/Permeabilization Solution Kit (BD Biosciences, catalog 554714), and stained with antibodies for intracellular cytokine assessment (see the "Flow cytometry" section) in the BD Perm/Wash buffer (BD Biosciences, catalog 554714) as per the manufacturer's protocol.

Flow cytometry

Cells were prepared from various tissues and stained with extracellular antibodies in FACS buffer (2% HI FBS, 1mM EDTA in 1× PBS without Mg^{2+}/Ca^{2+}). Antibodies are listed in supplemental table (data S11). H-2D(b) LCMV GP33-41 tetramer KAVYNFATM-APC was provided by the NIH tetramer core. Cells were stained at 4°C followed by fixation and permeabilization with appropriate intracellular staining kit. For intracellular staining of cytokines, the Cytofix/Cytoperm Fixation/Permeabilization Solution Kit from BD Biosciences was used as per the manufacturer's protocol. For intracellular staining of transcription factors, the FoxP3/Transcription Factor staining buffer set (eBioscience, catalog no. 00-5523-00) was used as per the manufacturer's protocol. To stain for transcription factors and preserve mCherry signal, cells were fixed

in Cytofix/Cytoperm and then permeabilized in FoxP3 perm buffer prior to overnight staining in the same buffer at 4C. Data were collected on a Symphony cytometer (BD Biosciences) and Northern Lights cytometer (Cytek).

Immunofluorescence Imaging

For multiplex imaging, tissue was fixed overnight at 4°C with paraformaldehyde-lysine-periodate fixative (PLP), subsequently dehydrated with 30% sucrose in PBS for 4 to 5 hours at 4 °C, and then embedded in cryomolds with 100% optimum cutting temperature (O.C.T.) compound (VWR, 25608-930) on dry ice for freezing. Tissue sections were rehydrated with PBS, then nonspecific binding sites were blocked with 3% BSA for 1 hour at room temperature. Slides were washed with PBST (PBS with 0.01% Tween20), stained with DAPI solution and autofluorescence images were acquired with Leica Cell Dive image system. Slides were stained with 1:100 diluted direct conjugated antibodies in separate staining rounds, including B220-AF488 (RA3-6B2, Biolegend, 103225); F480-Spark570 (BM8, Biolegend,123160); CD90.1-AF488 (OX-7, Biolegend, 202506); CD45.1-AF647(A20, Biolegend, 110720). Fluorescence was quenched by dye-inactivation solution after each round of staining. Imaging workflow followed Leica Cell DIVE multiplex imaging solution, and image results were analyzed by HALO AI image analysis software (Indica Labs).

Single-cell RNA sequencing

To generate the LCMV map data, H2D^b-gp33 specific CD8 T cells were sorted from the spleens of mice infected with acute or chronic LCMV at days 4, 8, 28, and 40 after infection. Days 4, 8, and 40 from both infections were sorted and submitted for 10X library prep together, whereas day 28 samples from both infections were performed separately. This denoted the "batch" assigned for downstream analysis (see analysis section). Each sample was loaded into its own Chromium instrument lane for 5′ scRNA library prep. Resulting library preps were sequenced on an Illumina Novaseq at a depth of 20,000 reads per cell. Library preparation and sequencing was performed according to manufacturer's instructions by the Yale Center for Genome Analysis (5′ v2 single-cell RNA sequencing, 10X Genomics) (YCGA) the same day as sample collection. Data was processed with cellranger-7.1.0 using the mm10 reference genome.

To generate the perturbSEQ data, transduced P14 DsRED Cas9 T cells and endogenous H2D^b-gp33 specific endogenous CD8 T cells were sorted out of the spleens of acute LCMV infected mice at day 8. They were then mixed at a 1:10 ratio and submitted for 5′ 10X Genomics scRNA and CRISPR library preparation. In total 240,000 cells were loaded onto six lanes of a ChromiumX instrument. Resulting library preps were se-

quenced on an Illumina NovaSeq at a depth of 20,000 reads per cell for the RNA library and 5000 reads per cells for the CRISPR library. Library preparation and sequencing was performed according to manufacturer's instructions by the Yale Center for Genome Analysis (5′ v2 scRNA-seq with feature barcode technology for CRISPR screening, 10X Genomics) was performed by the Yale Center for Genome Analysis (YCGA) the same day as sample collection. Data was processed with cellranger-7.1.0 using a custom reference transcriptome that added the DsRED RNA sequences to the mm10 reference genome to distinguish P14 from endogenous T cells.

scRNA-seq data of endogenous H2D^b-gp33 specific CD8 T cells from KP-NINJA tumor-bearing mice was generated as described in the original paper. ([42])

Single-cell RNA analysis

5′ scRNA-seq from sorted H2D^b-gp33 specific CD8 T cells at days 4, 8, 28, and 40 after acute or chronic LCMV infection was processed with Cell Ranger 7.1.0 using the mm10 mouse genome indices from 10X Genomics. R (v4.2.1) was used for analysis and the packages Seurat (v4.3.0) ([93]), DoubletFinder (v2.0.3) ([94]), and SingleR (v1.10.0) ([95]) were used to preprocess the data. Briefly, only cells with greater than 200 features and less than 5% mitochondrial reads were included. Further, the data was subset on predicted singlets as assigned by DoubletFinder and predicted T cells or NK cells as assigned by SingleR using the mouse bulk RNA-seq reference data (MouseRNAseqData) from celldex (v1.6.0). Cell cycle scoring was performed using Seurat's CellCycleScoring function. After these filtering steps we proceeded to analyze a total of 50,577 cells (6466 acute d4, 7163 acute d8, 9840 acute d28, 6630 acute d40, 6525 chronic d4, 7736 chronic d8, 1178 chronic d28, 5039 chronic d40). Cells were split into batch and cycling versus noncycling status prior to data integration through the IntegrateData function using the noncycling cells as the anchorset. Variable TCR, variable B cell receptor, mitochondrial, and cell cycle genes were excluded from integration features. This integration assay was then scaled and PCA was run. FindNeighbors was then run with PCA dimensions 1 through 8. FindClusters was run with a resolution of 0.35. RunUMAP was then performed using PCA dimensions 1 through 8, min.dist of 0.08 and n.components of 3L to generate 3D UMAP reduction. Clusters were assigned names based on gene module enrichment for previously defined CD8 T cell clusters. ([18]) Gene module enrichment was performed using the function AddModuleScore. Differentially expressed genes were calculated using the functions FindAllMarkers or FindMarkers for pairwise comparisons. The package dittoSeq (v1.8.1) was also used for some visualizations.

Monocle3 (v1.2.9) (*96*) was used to infer pseudotime on cells from either acute or chronic infection separately using SeuratWrappers (v0.3.0) and setting those cells with highest *Ccr7* expression as the root node.

5′ scRNA-seq with CRISPR from sorted transduced P14 DsRED Cas9 and endogenous H2D^b-gp33 T cells was processed with Cell Ranger 7.1.0 using the mm10 mouse genome indices from 10X Genomics with DsRED added as an additional feature. Cells were preprocessed and filtered as above, integrating across lanes and cell cycle status. We added an additional step to only analyze cells that contained a sgRNA feature. DsRED was also removed from integration features on top of variable TCR, variable BCR, mitochondrial, and cell cycle genes. A total of 59,815 cells were analyzed. The integrated assay was scaled and PCA was performed. FindNeighbors was performed using PCA dimensions 1 through 10. FindClusters was run with a resolution of 0.2. RunUMAP was then performed using PCA dimensions 1 through 10, a min.dist of 0.1, and n.components of 3L. PHATE reduction was performed using phateR and the integrated assay. The phate function was run using 50 PCA dimensions, knn of 10, and ndim of 3. Cells were assigned to a perturbation by first filtering out any cells that only had one sgRNA UMI captured to help correct for any ambient contamination. We then identified whether any sgRNA was captured, as a total of 80% or more of all sgRNA UMIs in the cell. Cells that did not meet this criterion were labeled as "inconclusive." Cells that were assigned a prominent sgRNA with this method were then assigned a perturbation label based on the target gene of that prominent sgRNA. For perturbation specific analysis, cells from all three sgRNA or all six sgRNAs (NTC) were pooled together. Gene modules derived from perturbSeq clusters were based on DEGs for each cluster using FindAllMarkers. KLF2 KO gene module was derived from DEGs between sgKLF2 and sgNTC cells using FindMarkers. Prediction of clusters in the LCMV map data was performed using the functions FindTransferAnchors, TransferData, and IntegrateEmbeddings using the integrated assay for each dataset. The packages EnhancedVolcano (v1.14.0) and pheatmap (v1.0.12) were used for additional visualizations.

5′ scRNA-seq of endogenous H2D^b-gp33 T cells in KP-NINJA tumor mice was initially processed through Cell Ranger as in the original paper (*42*). The four samples (dLN, tumor, week8, week17) were merged and were preprocessed and filtered to remove any contaminating B or myeloid cells based on canonical gene expression. Data was normalized and scaled (regressing out mitochondrial reads and number of RNA reads) and variable TCR sequences were removed from variable features used for PCA analysis. FindNeighbors was performed with PCA dimensions 1 through 20, FindClusters

was performed with a resolution of 0.5, and RunUMAP was performed with PCA dimensions 1 through 20. Gene module enrichment was performed used AddModuleScore and heatmap visualization was performed with pheatmap (v1.0.12).

Regulons were computed using the SCENIC pipeline (*97*). A gene regulatory network was inferred from negative control cells in the perturbSeq cells batch using Arboreto, a gradient boosting method (*98*). This resulted in a list of TF regulators for each gene in the data, weighted by the importance that the TF has in the prediction of the target. Modules were generated from this regulatory interaction, with each module comprising a TF and a list of predicted target genes). Multiple parallel strategies were used for the creation of the module:

Based on the top N targets for each factor (we used 50 targets).

Based on the top N regulators for a target (we used 5, 10, and 50 regulators).

Based on a percentile score (we used the 75th and 90th percentile of a factor's targets).

Modules with less than 20 genes were discarded for stability reasons. Modules were subsequently filtered using a cisTarget motif enrichment procedure. We jointly used two whole-genome rankings databases for *Mus musculus* (mm10) with a search space around the transcription start site of the genes of 500 bp upstream and 100 bp downstream as well as 10,000 bp upstream and 10,000 bp downstream, respectively. The sets of predicted direct target genes across all modules sharing the same regulator were then combined into a single regulon. Lastly, we computed the activity of a regulon in each individual cell. Each individual cell's transcriptome was used as a whole genome ranking based on the expression of its genes. The enrichment of a regulon was assessed via recovery of its targetome on the cell's whole-genome ranking. The resulting metric measured the biological activity of a regulon in each cell.

RNA Velocity analyses was performed as follows. The BAM files from cell ranger output were used as input into the velocyto.py pipeline (v0.17.17) to generate .loom files for each sample (*99*). The .loom files and the Seurat object, were then used for RNA velocity trajectory estimation using the scVelo tool (v0.2.5) (*99*, *100*). Genes that expressed less than 20 spliced and unspliced mRNA counts were filtered out during the normalization step. To compute moments for velocity estimation PCs 1 through 20 and 20 neighbors were considered with the umap method. Velocity was estimated using the 'stochastic' mode. The scVelo velocity stream was plotted onto the UMAP obtained from the Seurat analysis. The *scv.tl. rank_velocity_genes()* function in scVelo was used to identify genes with differential velocity across Seurat clusters.

Bulk ATAC-seq Preparation and Analysis

Control and KLF2 KO P14s were generated as described above and transferred into mice subsequently infected with LCMV ARM (CTRL, KO) or LCMV CL13 (CTRL). Spleens were pooled from respective infection cohorts and P14s were sorted out at day 8 post-infection and cryopreserved in 2 technical replicates in 90:10 FBS:DMSO prior to ATAC-seq library preparation. Samples were sequenced at a depth of 50M reads per sample on an Illumina NovaSeq instrument.

Bulk ATAC-seq processing

The study is comprised of three sample groups, each with two replicates (n = 6 total). Quality control (QC) for each sample was assessed using the MultiQC report generated by the nf-core atacseq pipeline (v2.1.2). Bulk ATAC-seq data was processed according to a published ATAC-seq pipeline (*101*). This pipeline included alignment of FASTQ files to the mm10 genome (Bowtie2), sorting and indexing of reads (samtools), removal of mitochondrial DNA reads, filtering for properly paired reads, estimation of library complexity (ATACseqQC), and subsampling to maintain comparable complexity across samples, PCR duplicate removal (Picard) and read mate fixing (samtools). BAM files were converted to BEDPE format (bedtools), and coordinates were shifted +4 and –5 bp for positive and negative strands, respectively, to compensate for Tn5 insertion. Broad peaks were called using MACS2 followed by removal of ENCODE blacklist regions (*102*) and unplaced contigs (bedtools).

Differentially accessible peak analysis

Differentially accessible peak (DAP) analysis was conducted according to the csaw_workflow portion of the Reske *et al.* pipeline, using R packages csaw, edgeR, and limma. (*101*) DAP was conducted across three comparisons: KLF2 KO vs WT (both Day 8 Acute), WT (Day 8 Acute) vs WT (Day 8 Chronic), and KLF2 KO (Day 8 Acute) vs WT (Day 8 Chronic). The peaks called in the previous step were used as input. Preprocessing involved removing low abundance peaks and generating a count matrix (p × m) for each comparison, where p represented the number of peaks (48,364) identified from a consensus peak set defined based on a union of peaks from all samples. Each pairwise comparison included four samples (m = 4), representing two replicates per condition. Peaks were normalized using loess normalization. Different normalization methods, including TMM normalization, were applied and the results were robust. Subsequently peaks within 500 bp of each other were merged with the maximum merged peak width is ≤5000 bp. DAPs in each comparison were identified using the estimateDisp, glmQLFit, and glmQLFTest functions from edgeR and

defined as significant if the false discovery rate was <0.05.

Differential TF activity analysis

TF activities were inferred using chromVAR (*103*), which convolves TF binding motif score with peak accessibility. Differences in inferred chromVAR TF activities were computed for each comparison, utilizing the JASPAR2020 motif database. Raw peak count matrices were used as the input and chromVAR was run using default parameters. TF activities (corresponding to motifs) were considered significantly different if adjusted $P < 0.05$.

Statistical analyses

All statistical analyses were performed using Prism V10.2.2 software or R software. Normality was tested before using analysis of variance (ANOVA), t test, or Wilcoxon rank sum test. In the case where datapoints were derived from the same animal, as in our P14 cotransfers, paired statistical tests were performed. Data are shown as individual data points with statistical significance indicating comparison of mean unless otherwise noted. Randomization was performed for tumor growth experiment at time of P14 transfer. In figure legends, n indicates the number of animals in in vivo experiments or biological replicates, where applicable. Sample size was determined by smaller pilot experiments or was informed by previous experience. Significance was denoted as follows: *$P < 0.05$; **$P < 0.01$; ***$P < 0.001$; ****$P < 0.0001$.

REFERENCES AND NOTES

1. D. E. Speiser et al., T cell differentiation in chronic infection and cancer: Functional adaptation or exhaustion? Nat. Rev. Immunol. 14, 768–774 (2014). doi: 10.1038/nri3740; pmid: 25257362
2. M. Philip, A. Schietinger, CD8+ T cell differentiation and dysfunction in cancer. Nat. Rev. Immunol. 22, 209–223 (2022). doi: 10.1038/s41577-021-00574-3; pmid: 34253904
3. X. Lan, C. C. Zebley, B. Youngblood, Cellular and molecular waypoints along the path of T cell exhaustion. Sci. Immunol. 8, eadg3868 (2023). doi: 10.1126/sciimmunol.adg3868; pmid: 37656775
4. L. Kok, D. Masopust, T. N. Schumacher, The precursors of CD8+ tissue resident memory T cells: From lymphoid organs to infected tissues. Nat. Rev. Immunol. 22, 283–293 (2022). doi: 10.1038/s41577-021-00590-3; pmid: 34480118
5. T. Gebhardt, S. L. Park, I. A. Parish, Stem-like exhausted and memory CD8+ T cells in cancer. Nat. Rev. Cancer 23, 780–798 (2023). doi: 10.1038/s41568-023-00615-0; pmid: 37821656
6. M. Buggert, D. A. Price, L. K. Mackay, M. R. Betts, Human circulating and tissue-resident memory CD8+ T cells. Nat. Immunol. 24, 1076–1086 (2023). doi: 10.1038/s41590-023-01538-6; pmid: 37349380
7. S. Sarkar et al., Functional and genomic profiling of effector CD8 T cell subsets with distinct memory fates. J. Exp. Med. 205, 625–640 (2008). doi: 10.1084/jem.20071641; pmid: 18316415
8. N. S. Joshi et al., Inflammation directs memory precursor and short-lived effector CD8(+) T cell fates via the graded expression of T-bet transcription factor. Immunity 27, 281–295 (2007). doi: 10.1016/j.immuni.2007.07.010; pmid: 17723218
9. B. Youngblood et al., Effector CD8 T cells dedifferentiate into long-lived memory cells. Nature 552, 404–409 (2017). doi: 10.1038/nature25144; pmid: 29236683
10. D. Zehn, R. Thimme, E. Lugli, G. P. de Almeida, A. Oxenius, 'Stem-like' precursors are the fount to sustain persistent CD8+ T cell responses. Nat. Immunol. 23, 836–847 (2022). doi: 10.1038/s41590-022-01219-w; pmid: 35624209
11. J. R. Giles, A. M. Globig, S. M. Kaech, E. J. Wherry, CD8+ T cells in the cancer-immunity cycle. Immunity 56, 2231–2253 (2023). doi: 10.1016/j.immuni.2023.09.005; pmid: 37820583
12. L. M. McLane, M. S. Abdel-Hakeem, E. J. Wherry, CD8 T Cell Exhaustion During Chronic Viral Infection and Cancer. Annu. Rev. Immunol. 37, 457–495 (2019). doi: 10.1146/annurev-immunol-041015-055318; pmid: 30676822
13. Z. Chen et al., TCF-1-Centered Transcriptional Network Drives an Effector versus Exhausted CD8 T Cell-Fate Decision. Immunity 51, 840–855.e5 (2019). doi: 10.1016/j.immuni.2019.09.013; pmid: 31606264
14. S. N. Mueller, L. K. Mackay, Tissue-resident memory T cells: Local specialists in immune defence. Nat. Rev. Immunol. 16, 79–89 (2016). doi: 10.1038/nri.2015.3; pmid: 26688350
15. P. A. Szabo, M. Miron, D. L. Farber, Location, location, location: Tissue resident memory T cells in mice and humans. Sci. Immunol. 4, eaas9673 (2019). doi: 10.1126/sciimmunol.aas9673; pmid: 30952804
16. M. Y. Kasmani et al., Clonal lineage tracing reveals mechanisms skewing CD8+ T cell fate decisions in chronic infection. J. Exp. Med. 220, e20220679 (2023). doi: 10.1084/jem.20220679; pmid: 36315049
17. J. E. Mold et al., Divergent clonal differentiation trajectories establish CD8+ memory T cell heterogeneity during acute viral infections in humans. Cell Rep. 35, 109174 (2021). doi: 10.1016/j.celrep.2021.109174; pmid: 34038736
18. B. Daniel et al., Divergent clonal differentiation trajectories of T cell exhaustion. Nat. Immunol. 23, 1614–1627 (2022). doi: 10.1038/s41590-022-01337-5; pmid: 36289450
19. A. E. Baxter et al., The SWI/SNF chromatin remodeling complexes BAF and PBAF differentially regulate epigenetic transitions in exhausted CD8+ T cells. Immunity 56, 1320–1340.e10 (2023). doi: 10.1016/j.immuni.2023.05.008; pmid: 37315535
20. A. Kharel et al., Loss of PBAF promotes expansion and effector differentiation of CD8+ T cells during chronic viral infection and cancer. Cell Rep. 42, 112649 (2023). doi: 10.1016/j.celrep.2023.112649; pmid: 37330910
21. G. Montacchiesi, L. Pace, Epigenetics and CD8+ T cell memory. Immunol. Rev. 305, 77–89 (2022). doi: 10.1111/imr.13057; pmid: 34923638
22. C. U. Blank et al., Defining 'T cell exhaustion'. Nat. Rev. Immunol. 19, 665–674 (2019). doi: 10.1038/s41577-019-0221-9; pmid: 31570879
23. A. N. Henning, R. Roychoudhuri, N. P. Restifo, Epigenetic control of CD8+ T cell differentiation. Nat. Rev. Immunol. 18, 340–356 (2018). doi: 10.1038/nri.2017.146; pmid: 29379213
24. A. Guo et al., cBAF complex components and MYC cooperate early in CD8+ T cell fate. Nature 607, 135–141 (2022). doi: 10.1038/s41586-022-04849-0; pmid: 35732731
25. J. C. Beltra et al., Developmental Relationships of Four Exhausted CD8+ T Cell Subsets Reveals Underlying Transcriptional and Epigenetic Landscape Control Mechanisms. Immunity 52, 825–841.e8 (2020). doi: 10.1016/j.immuni.2020.04.014; pmid: 32396847
26. J. R. Giles et al., Shared and distinct biological circuits in effector, memory and exhausted CD8+ T cells revealed by temporal single-cell transcriptomics and epigenetics. Nat. Immunol. 23, 1600–1613 (2022). doi: 10.1038/s41590-022-01338-4; pmid: 36271148
27. B. Kakaradov et al., Early transcriptional and epigenetic regulation of CD8+ T cell differentiation revealed by single-cell RNA sequencing. Nat. Immunol. 18, 422–432 (2017). doi: 10.1038/ni.3688; pmid: 28218746
28. J. M. Replogle et al., Mapping information-rich genotype-phenotype landscapes with genome-scale Perturb-seq. Cell 185, 2559–2575.e28 (2022). doi: 10.1016/j.cell.2022.05.013; pmid: 35688146
29. A. Dixit et al., Perturb-Seq: Dissecting Molecular Circuits with Scalable Single-Cell RNA Profiling of Pooled Genetic Screens. Cell 167, 1853–1866.e17 (2016). doi: 10.1016/j.cell.2016.11.038; pmid: 27984732
30. J. A. Belk et al., Genome-wide CRISPR screens of T cell exhaustion identify chromatin remodeling factors that limit T cell persistence. Cancer Cell 40, 768–786.e7 (2022). doi: 10.1016/j.ccell.2022.06.001; pmid: 35750052
31. P. Zhou et al., Single-cell CRISPR screens in vivo map T cell fate regulomes in cancer. Nature 624, 154–163 (2023). doi: 10.1038/s41586-023-06733-x; pmid: 37968405
32. W. Zhou, F. Gao, M. Romero-Wolf, S. Jo, E. V. Rothenberg, Single-cell deletion analyses show control of pro-T cell developmental speed and pathways by Tcf7, Spi1, Gata3, Bcl11a, Erg, and Bcl11b. Sci. Immunol. 7, eabm1920 (2022). doi: 10.1126/sciimmunol.abm1920; pmid: 35594339
33. E. J. Wherry, J. N. Blattman, K. Murali-Krishna, R. van der Most, R. Ahmed, Viral persistence alters CD8 T-cell immunodominance and tissue distribution and results in distinct stages of functional impairment. J. Virol. 77, 4911–4927 (2003). doi: 10.1128/JVI.77.8.4911-4927.2003; pmid: 12663797
34. T. Yajima et al., IL-15 regulates CD8+ T cell contraction during primary infection. J. Immunol. 176, 507–515 (2006). doi: 10.4049/jimmunol.176.1.507; pmid: 16365444
35. J. E. Kohlmeier et al., Inflammatory chemokine receptors regulate CD8(+) T cell contraction and memory generation following infection. J. Exp. Med. 208, 1621–1634 (2011). doi: 10.1084/jem.20102110; pmid: 21788409
36. D. T. Utzschneider et al., Early precursor T cells establish and propagate T cell exhaustion in chronic infection. Nat. Immunol. 21, 1256–1266 (2020). doi: 10.1038/s41590-020-0760-z; pmid: 32839610
37. O. Khan et al., TOX transcriptionally and epigenetically programs CD8+ T cell exhaustion. Nature 571, 211–218 (2019). doi: 10.1038/s41586-019-1325-x; pmid: 31207603
38. A. C. Scott et al., TOX is a critical regulator of tumour-specific T cell differentiation. Nature 571, 270–274 (2019). doi: 10.1038/s41586-019-1324-y; pmid: 31207604
39. C. Yao et al., Single-cell RNA-seq reveals TOX as a key regulator of CD8+ T cell persistence in chronic infection. Nat. Immunol. 20, 890–901 (2019). doi: 10.1038/s41590-019-0403-4; pmid: 31209400
40. R. Zander, W. Cui, Exhausted CD8+ T cells face a developmental fork in the road. Trends Immunol. 44, 276–286 (2023). doi: 10.1016/j.it.2023.02.006; pmid: 36907685
41. R. Zander et al., CD4+ T Cell Help Is Required for the Formation of a Cytolytic CD8+ T Cell Subset that Protects against Chronic Infection and Cancer. Immunity 51, 1028–1042.e4 (2019). doi: 10.1016/j.immuni.2019.10.009; pmid: 31810883
42. K. A. Connolly et al., A reservoir of stem-like CD8+ T cells in the tumor-draining lymph node preserves the ongoing antitumor immune response. Sci. Immunol. 6, eabg7836 (2021). doi: 10.1126/sciimmunol.abg7836; pmid: 34597124
43. R. Tuladhar et al., CRISPR-Cas9-based mutagenesis frequently provokes on-target mRNA misregulation. Nat. Commun. 10, 4056 (2019). doi: 10.1038/s41467-019-12028-5; pmid: 31492834
44. J. L. Anderson et al., mRNA processing in mutant zebrafish lines generated by chemical and CRISPR-mediated mutagenesis produces unexpected transcripts that escape nonsense-mediated decay. PLOS Genet. 13, e1007105 (2017). doi: 10.1371/journal.pgen.1007105; pmid: 29161261
45. A. Xin et al., A molecular threshold for effector CD8(+) T cell differentiation controlled by transcription factors Blimp-1 and T-bet. Nat. Immunol. 17, 422–432 (2016). doi: 10.1038/ni.3410; pmid: 26950239
46. R. L. Rutishauser et al., Transcriptional repressor Blimp-1 promotes CD8(+) T cell terminal differentiation and represses the acquisition of central memory T cell properties. Immunity 31, 296–308 (2009). doi: 10.1016/j.immuni.2009.05.014; pmid: 19664941
47. K. D. Omilusik et al., Transcriptional repressor ZEB2 promotes terminal differentiation of CD8+ effector and memory T cell populations during infection. J. Exp. Med. 212, 2027–2039 (2015). doi: 10.1084/jem.20150194; pmid: 26503445
48. F. Masson et al., Id2-mediated inhibition of E2A represses memory CD8+ T cell differentiation. J. Immunol. 190, 4585–4594 (2013). doi: 10.4049/jimmunol.1300099; pmid: 23536629
49. D. Herndler-Brandstetter et al., KLRG1+ Effector CD8+ T Cells Lose KLRG1, Differentiate into All Memory T Cell Lineages, and Convey Enhanced Protective Immunity. Immunity 48, 716–729.e8 (2018). doi: 10.1016/j.immuni.2018.03.015; pmid: 29625895
50. C. Yao et al., BACH2 enforces the transcriptional and epigenetic programs of stem-like CD8+ T cells. Nat. Immunol. 22, 370–380 (2021). doi: 10.1038/s41590-021-00868-7; pmid: 33574619
51. X. Zhou, H.-H. Xue, Cutting edge: Generation of memory precursors and functional memory CD8+ T cells depends on T cell factor-1 and lymphoid enhancer-binding factor-1. J. Immunol. 189, 2722–2726 (2012). doi: 10.4049/jimmunol.1201150; pmid: 22875805

52. D. Pais Ferreira et al., Central memory CD8+ T cells derive from stem-like Tcf7hi effector cells in the absence of cytotoxic differentiation. Immunity 53, 985–1000.e11 (2020). doi: 10.1016/j.immuni.2020.09.005; pmid: 33128876

53. J. G. Silva et al., Emergence and fate of stem cell-like Tcf7+ CD8+ T cells during a primary immune response to viral infection. Sci. Immunol. 8, eadh3113 (2023). doi: 10.1126/sciimmunol.adh3113; pmid: 37976346

54. L. K. Quezada et al., Early transcriptional and epigenetic divergence of CD8+ T cells responding to acute versus chronic infection. PLOS Biol. 21, e3001983 (2023). doi: 10.1371/journal.pbio.3001983; pmid: 36716323

55. S. M. Gray, R. A. Amezquita, T. Guan, S. H. Kleinstein, S. M. Kaech, Polycomb Repressive Complex 2-Mediated Chromatin Repression Guides Effector CD8+ T Cell Terminal Differentiation and Loss of Multipotency. Immunity 46, 596–608 (2017). doi: 10.1016/j.immuni.2017.03.012; pmid: 28410989

56. K. R. Moon et al., Visualizing structure and transitions in high-dimensional biological data. Nat. Biotechnol. 37, 1482–1492 (2019). doi: 10.1038/s41587-019-0336-3; pmid: 31796933

57. M. S. Strine et al., Intestinal tuft cell immune privilege enables norovirus persistence. Sci. Immunol. 9, eadi7038 (2024). doi: 10.1126/sciimmunol.adi7038; pmid: 38517952

58. J. Wittner, W. Schuh, Krüppel-like Factor 2 (KLF2) in Immune Cell Migration. Vaccines 9, 1171 (2021). doi: 10.3390/vaccines9101171; pmid: 34696279

59. Y. Chen et al., BATF regulates progenitor to cytolytic effector CD8+ T cell transition during chronic viral infection. Nat. Immunol. 22, 996–1007 (2021). doi: 10.1038/s41590-021-00965-7; pmid: 34282329

60. M. S. Abdel-Hakeem et al., Epigenetic scarring of exhausted T cells hinders memory differentiation upon eliminating chronic antigenic stimulation. Nat. Immunol. 22, 1008–1019 (2021). doi: 10.1038/s41590-021-00975-5; pmid: 34312545

61. Z. Zhu et al., FOXP1 and KLF2 reciprocally regulate checkpoints of stem-like to effector transition in CAR T cells. Nat. Immunol. (2023). pmid: 38012417

62. E. J. Wherry et al., Molecular signature of CD8+ T cell exhaustion during chronic viral infection. Immunity 27, 670–684 (2007). doi: 10.1016/j.immuni.2007.09.006; pmid: 17950003

63. K. Takada et al., Kruppel-like factor 2 is required for trafficking but not quiescence in postactivated T cells. J. Immunol. 186, 775–783 (2011). doi: 10.4049/jimmunol.1000094; pmid: 21160050

64. H. Shin, S. D. Blackburn, J. N. Blattman, E. J. Wherry, Viral antigen and extensive division maintain virus-specific CD8 T cells during chronic infection. J. Exp. Med. 204, 941–949 (2007). doi: 10.1084/jem.20061937; pmid: 17420267

65. J.-Y. Lee et al., The transcription factor KLF2 restrains CD4+ T follicular helper cell differentiation. Immunity 42, 252–264 (2015). doi: 10.1016/j.immuni.2015.01.013; pmid: 25692701

66. T. Vardam-Kaur et al., The Extracellular ATP Receptor P2RX7 Imprints a Promemory Transcriptional Signature in Effector CD8+ T Cells. J. Immunol. 208, 1686–1699 (2022). doi: 10.4049/jimmunol.2100555; pmid: 35264459

67. H. Borges da Silva et al., Sensing of ATP via the Purinergic Receptor P2RX7 Promotes CD8+ Trm Cell Generation by Enhancing Their Sensitivity to the Cytokine TGF-β. Immunity 53, 158–171.e6 (2020). doi: 10.1016/j.immuni.2020.06.010; pmid: 32640257

68. K. Abadie et al., Reversible, tunable epigenetic silencing of TCF1 generates flexibility in the T cell memory decision. Immunity 57, 271–286.e13 (2024). doi: 10.1016/j.immuni.2023.12.006; pmid: 38301652

69. N. Lam, Y. Lee, D. L. Farber, A guide to adaptive immune memory. Nat. Rev. Immunol. 24, 810–829 (2024). doi: 10.1038/s41577-024-01040-6; pmid: 38831162

70. B. T. Endrizzi, S. C. Jameson, Differential role for IL-7 in inducing lung Kruppel-like factor (Kruppel-like factor 2) expression by naive versus activated T cells. Int. Immunol. 15, 1341–1348 (2003). doi: 10.1093/intimm/dxg133; pmid: 14565932

71. S. L. Schober et al., Expression of the transcription factor lung Krüppel-like factor is regulated by cytokines and correlates with survival of memory T cells in vitro and in vivo. J. Immunol. 163, 3662–3667 (1999). doi: 10.4049/jimmunol.163.7.3662; pmid: 10490960

72. G. C. Preston, C. Feijoo-Carnero, N. Schurch, V. H. Cowling, D. A. Cantrell, The impact of KLF2 modulation on the transcriptional program and function of CD8 T cells. PLOS ONE 8, e77537 (2013). doi: 10.1371/journal.pone.0077537; pmid: 24155966

73. T. Yamada, C. S. Park, M. Mamonkin, H. D. Lacorazza, Transcription factor ELF4 controls the proliferation and homing of CD8+ T cells via the Krüppel-like factors KLF4 and KLF2. Nat. Immunol. 10, 618–626 (2009). doi: 10.1038/ni.1730; pmid: 19412182

74. C. Tsui et al., MYB orchestrates T cell exhaustion and response to checkpoint inhibition. Nature 609, 354–360 (2022). doi: 10.1038/s41586-022-05105-1; pmid: 35978192

75. Q. Huang et al., The primordial differentiation of tumor-specific memory CD8+ T cells as bona fide responders to PD-1/PD-L1 blockade in draining lymph nodes. Cell 185, 4049–4066.e25 (2022). doi: 10.1016/j.cell.2022.09.020; pmid: 36208623

76. B. Fitzgerald et al., A mouse model for the study of anti-tumor T cell responses in Kras-driven lung adenocarcinoma. Cell Rep. Methods 1, 100080 (2021). doi: 10.1016/j.crmeth.2021.100080; pmid: 34632444

77. A. K. Molodtsov et al., Resident memory CD8+ T cells in regional lymph nodes mediate immunity to metastatic melanoma. Immunity 54, 2117–2132.e7 (2021). doi: 10.1016/j.immuni.2021.08.019; pmid: 34525340

78. I. Sandu et al., Landscape of Exhausted Virus-Specific CD8 T Cells in Chronic LCMV Infection. Cell Rep. 32, 108078 (2020). doi: 10.1016/j.celrep.2020.108078; pmid: 32846135

79. W. H. Hudson et al., Proliferating Transitory T Cells with an Effector-like Transcriptional Signature Emerge from PD-1+ Stem-like CD8+ T Cells during Chronic Infection. Immunity 51, 1043–1058.e4 (2019). doi: 10.1016/j.immuni.2019.11.002; pmid: 31810882

80. D. Riegel et al., Integrated single-cell profiling dissects cell-state-specific enhancer landscapes of human tumor-infiltrating CD8+ T cells. Mol. Cell 83, 622–636.e10 (2023). doi: 10.1016/j.molcel.2022.12.029; pmid: 36657444

81. M. A. Weinreich et al., KLF2 transcription-factor deficiency in T cells results in unrestrained cytokine production and upregulation of bystander chemokine receptors. Immunity 31, 122–130 (2009). doi: 10.1016/j.immuni.2009.05.011; pmid: 19592277

82. A. Bai, H. Hu, M. Yeung, J. Chen, Kruppel-like factor 2 controls T cell trafficking by activating L-selectin (CD62L) and sphingosine-1-phosphate receptor 1 transcription. J. Immunol. 178, 7632–7639 (2007). doi: 10.4049/jimmunol.178.12.7632; pmid: 17548599

83. C. N. Skon et al., Transcriptional downregulation of S1pr1 is required for the establishment of resident memory CD8+ T cells. Nat. Immunol. 14, 1285–1293 (2013). doi: 10.1038/ni.2745; pmid: 24162775

84. H. Shin et al., A role for the transcriptional repressor Blimp-1 in CD8(+) T cell exhaustion during chronic viral infection. Immunity 31, 309–320 (2009). doi: 10.1016/j.immuni.2009.06.019; pmid: 19664943

85. G. Xin et al., A Critical Role of IL-21-Induced BATF in Sustaining CD8-T-Cell-Mediated Chronic Viral Control. Cell Rep. 13, 1118–1124 (2015). doi: 10.1016/j.celrep.2015.09.069; pmid: 26527008

86. C. Kao et al., Transcription factor T-bet represses expression of the inhibitory receptor PD-1 and sustains virus-specific CD8+ T cell responses during chronic infection. Nat. Immunol. 12, 663–671 (2011). doi: 10.1038/ni.2046; pmid: 21623380

87. A. E. Denton, B. E. Russ, P. C. Doherty, S. Rao, S. J. Turner, Differentiation-dependent functional and epigenetic landscapes for cytokine genes in virus-specific CD8+ T cells. Proc. Natl. Acad. Sci. U.S.A. 108, 15306–15311 (2011). doi: 10.1073/pnas.1112520108; pmid: 21876173

88. J. M. Angelosanto, S. D. Blackburn, A. Crawford, E. J. Wherry, Progressive loss of memory T cell potential and commitment to exhaustion during chronic viral infection. J. Virol. 86, 8161–8170 (2012). doi: 10.1128/JVI.00889-12; pmid: 22623779

89. H. Pircher, K. Bürki, R. Lang, H. Hengartner, R. M. Zinkernagel, Tolerance induction in double specific T-cell receptor transgenic mice varies with antigen. Nature 342, 559–561 (1989). doi: 10.1038/342559a0; pmid: 2573841

90. S.-H. Chiou et al., Pancreatic cancer modeling using retrograde viral vector delivery and in vivo CRISPR/Cas9-mediated somatic genome editing. Genes Dev. 29, 1576–1585 (2015). doi: 10.1101/gad.264861.115; pmid: 26178787

91. K. Labun et al., CHOPCHOP v3: Expanding the CRISPR web toolbox beyond genome editing. Nucleic Acids Res. 47 (W1), W171–W174 (2019). doi: 10.1093/nar/gkz365; pmid: 31106871

92. S. Nüssing et al., Efficient CRISPR/Cas9 Gene Editing in Uncultured Naive Mouse T Cells for In Vivo Studies. J. Immunol. 204, 2308–2315 (2020). doi: 10.4049/jimmunol.1901396; pmid: 32152070

93. Y. Hao et al., Integrated analysis of multimodal single-cell data. Cell 184, 3573–3587.e29 (2021). doi: 10.1016/j.cell.2021.04.048; pmid: 34062119

94. C. S. McGinnis, L. M. Murrow, Z. J. Gartner, DoubletFinder: Doublet Detection in Single-Cell RNA Sequencing Data Using Artificial Nearest Neighbors. Cell Syst. 8, 329–337.e4 (2019). doi: 10.1016/j.cels.2019.03.003; pmid: 30954475

95. D. Aran et al., Reference-based analysis of lung single-cell sequencing reveals a transitional profibrotic macrophage. Nat. Immunol. 20, 163–172 (2019). doi: 10.1038/s41590-018-0276-y; pmid: 30643263

96. J. Cao et al., The single-cell transcriptional landscape of mammalian organogenesis. Nature 566, 496–502 (2019). doi: 10.1038/s41586-019-0969-x; pmid: 30787437

97. S. Aibar et al., SCENIC: Single-cell regulatory network inference and clustering. Nat. Methods 14, 1083–1086 (2017). doi: 10.1038/nmeth.4463; pmid: 28991892

98. T. Moerman et al., GRNBoost2 and Arboreto: Efficient and scalable inference of gene regulatory networks. Bioinformatics 35, 2159–2161 (2019). doi: 10.1093/bioinformatics/bty916; pmid: 30445495

99. V. Bergen, M. Lange, S. Peidli, F. A. Wolf, F. J. Theis, Generalizing RNA velocity to transient cell states through dynamical modeling. Nat. Biotechnol. 38, 1408–1414 (2020). doi: 10.1038/s41587-020-0591-3; pmid: 32747759

100. G. La Manno et al., RNA velocity of single cells. Nature 560, 494–498 (2018). doi: 10.1038/s41586-018-0414-6; pmid: 30089906

101. J. J. Reske, M. R. Wilson, R. L. Chandler, ATAC-seq normalization method can significantly affect differential accessibility analysis and interpretation. Epigenetics Chromatin 13, 22 (2020). doi: 10.1186/s13072-020-00342-y; pmid: 32321567

102. A. Boyle, Boyle-Lab/Blacklist: Official ENCODE Blacklist release for publication (v2.0), Zenodo (2018); https://doi.org/10.5281/zenodo.1491733.

103. A. N. Schep, B. Wu, J. D. Buenrostro, W. J. Greenleaf, chromVAR: Inferring transcription-factor-associated accessibility from single-cell epigenomic data. Nat. Methods 14, 975–978 (2017). doi: 10.1038/nmeth.4401; pmid: 28825706

104. E. Fagerberg, KLF2 maintains lineage fidelity and suppresses CD8 T cell exhaustion during acute LCMV infection (PerturbSeq Data), Dryad (2024); https://doi.org/10.5061/dryad.s7h44j1gr.

105. E. Fagerberg, KLF2 maintains lineage fidelity and suppresses CD8 T cell exhaustion during acute LCMV infection (LCMV DSM scRNA data and ATAC-seq), Dryad (2024); https://doi.org/10.5061/dryad.dv41ns27h.

SUPPLEMENTARY MATERIALS LIST

science.org/doi/10.1126/science.adn2337
Figs. S1 to S17
MDAR Reproducibility Checklist
Data S1 to S12